

**3-D FINITE ELEMENT MODELING OF SEQUENTIAL OBLIQUE CUTTING OF
UNIDIRECTIONAL CARBON FIBER REINFORCED POLYMER**

by

Xiaofan Xu

B.Eng., Beihang University, 2018

A THESIS SUBMITTED IN PARTIAL FULFILLMENT OF
THE REQUIREMENTS FOR THE DEGREE OF

MASTER OF APPLIED SCIENCE

in

THE FACULTY OF GRADUATE AND POSTDOCTORAL STUDIES

(Mechanical Engineering)

THE UNIVERSITY OF BRITISH COLUMBIA

(Vancouver)

September 2020

© Xiaofan Xu, 2020

The following individuals certify that they have read, and recommend to the Faculty of Graduate and Postdoctoral Studies for acceptance, a thesis entitled:

3-D Finite Element Modeling of Sequential Oblique Cutting of Unidirectional Carbon Fiber Reinforced Polymer

submitted by Xiaofan Xu in partial fulfillment of the requirements for

the degree of Master of Applied Science

in Mechanical Engineering

Examining Committee:

Dr. Xiaoliang Jin, Mechanical Engineering

Supervisor

Dr. Mauricio Ponga, Mechanical Engineering

Supervisory Committee Member

Dr. Reza Vaziri, Civil Engineering

Supervisory Committee Member

Abstract

Carbon fiber reinforced polymer (CFRP) composites have been widely used in aerospace, aviation, and automotive industries due to their high strength/stiffness-to-weight ratios, high temperature resistance and corrosion resistance. CFRP components are usually produced in near net-shape, and cutting operations such as drilling, slot milling, and edge trimming are required to remove excessive materials and fulfill the geometry and surface quality requirements of the final parts. Practical cutting operations are in the form of oblique and sequential cutting at the tool edge.

Different from metal cutting, the material removal mechanism and surface quality are highly dependent on the fiber orientation in cutting CFRP materials. This thesis presents a 3-D finite element model of oblique cutting of unidirectional CFRP. The effects of the fiber orientation and oblique angles on the chip formation, cutting forces, and subsurface damage are simulated and analyzed. It is found that the out-of-plane force and the depth of subsurface damage increase with the oblique angle in all fiber orientation angles except 0° . To represent the nature of sequential cutting, a second cut on the machined material with existing damages and residual stresses due to previous cutting is simulated. The results show that the effect of sequential cutting on the cutting forces is the largest at 90° fiber orientation angle.

Oblique cutting experiments were conducted on unidirectional CFRP. The cutting forces and chip morphology between the simulations and the experimental results were compared. The proposed FE model reveals the effect of oblique angle and sequential cutting on the mechanisms of chip formation and surface generation. The results are able to provide guidance in choosing proper cutting parameters and tool geometries to minimize the subsurface damage and potential delamination corresponding to in actual cutting operations of CFRP composites.

Lay Summary

Carbon fiber reinforced polymer composites (CFRP) are widely used in aerospace, aviation, and automotive industries due to their excellent mechanical properties. Practical machining operations used in industry such as milling and drilling always involve oblique cutting at the tool tip, that the cutting tool edge is not perpendicular to the direction of cutting velocity. Moreover, the cutting process produces damages and residual stresses at the machined surface, which influence the chip formation and cutting forces in subsequent cutting operations. This thesis presents a three-dimensional finite element model of cutting CFRP considering these effects. The geometry of the machined chips, the cutting forces, and the machined surface quality are analyzed. Cutting experiments were performed to verify the model. The results explain the mechanism of cutting process which is closer to practical cutting operations, and are able to provide guidance for choosing proper cutting parameters and cutting tool geometries.

Preface

This dissertation is original, unpublished, independent work by the author, Xiaofan Xu. He is responsible for conducting all the simulations, experiments and completing the analyses in this thesis. Dr. Xiaoliang Jin is the supervisor for this work.

Table of Contents

Abstract.....	iii
Lay Summary	iv
Preface.....	v
Table of Contents	vi
List of Tables	ix
List of Figures.....	x
List of Symbols	xv
List of Abbreviations	xvii
Acknowledgements	xviii
Chapter 1: Introduction	1
1.1 Background.....	1
1.2 Structure of carbon fiber reinforced polymer	3
1.2.1 Carbon fiber	3
1.2.2 Matrix.....	5
1.3 Machining of CFRP	6
1.3.1 Characteristics of machining CFRP	6
1.3.2 Orthogonal and oblique cutting	7
1.3.3 Milling of CFRP	9
1.4 Research objective	10
Chapter 2: Literature review	12
2.1 Analytical studies.....	12

2.1.1	Macro-mechanical analytical models	12
2.1.2	Micro-mechanical analytical models	18
2.2	Experimental studies.....	25
2.3	Numerical studies.....	28
2.3.1	Macro-mechanical numerical modeling	29
2.3.2	Micro-mechanical numerical modeling	32
2.4	Oblique cutting theory for metal alloys	39
Chapter 3: Finite Element Modeling.....		41
3.1	Geometry and Process Parameters in the FE model.....	41
3.2	Material definition in the FE model.....	44
3.2.1	Carbon Fiber	44
3.2.2	Matrix.....	45
3.2.3	Fiber-matrix interface	46
Chapter 4: Simulations and Experimental Verification.....		49
4.1	Experimental setup.....	49
4.2	Simulations and experimental comparison	51
4.2.1	Chip formation	52
4.2.2	Cutting forces.....	59
Chapter 5: Analyses and discussions		65
5.1	Effect of oblique angle on surface generation	65
5.2	Effect of sequential cutting	69
5.3	Effect of random fiber distribution on cutting forces	73
Chapter 6: Conclusion and future work.....		76

6.1	Conclusion	76
6.2	Future work.....	78
	Bibliography	79

List of Tables

Table 1 Parameters used in the FE model and simulations.....	43
Table 2 Mechanical properties of the UD- CFRP workpiece defined in FE model.....	48
Table 3 Comparison of cutting forces between workpiece with uniform and random distribution of fibers for $\theta=45^\circ$ and $i = 15^\circ$ and $i = 45^\circ$	75

List of Figures

Figure 1.1: (a) Edge trimming and (b) drilling operations of CFRP.....	02
Figure 1.2: Delamination and burrs in (a) drilling [1], (b) milling [1] and (c) oblique cutting process.....	02
Figure 1.3: Schematic of different reinforcement arrangements in composites [3].....	04
Figure 1.4: Typical powder-like chips formed in orthogonal cutting experiment [4].....	07
Figure 1.5: Typical aluminum chips formed in milling process [5].....	07
Figure 1.6: Schematic illustration of (a) orthogonal cutting and (b) oblique cutting [7].....	08
Figure 1.7: (a) Milling process of CFRP and helix angle definition and (b) oblique cutting of UD-CFRP	10
Figure 1.8: Sequential cutting of UD-CFRP workpiece.....	11
Figure 2.1: (a) Initial configuration and (b) deformation of the chip of Everstine and Rogers model [8]	13
Figure 2.2: Orthogonal cutting model of FRP from Takeyama and Iijima [9].....	14
Figure 2.3: Comparison of experimental and calculated data for (a) principal and (b) thrust force from Takeyama and Iijima [9] model.....	15
Figure 2.4: Definitions of the deformation zones [11].....	16
Figure 2.5: Comparison between model predictions and experimental measurements [11].....	18
Figure 2.6: Stress distribution of a fiber during orthogonal cutting of UD-FRP [14].....	19
Figure 2.7: (a) Three regions in orthogonal cutting; (b) Load condition of RVE [11].....	21

Figure 2.8: Theoretical and experimental cutting and thrust forces versus fiber orientation with: (a) $\gamma = 10^\circ$ and $a_c = 0.1$ mm; (b) $\gamma = 20^\circ$ and $a_c = 0.1$ mm; (c) $\gamma = 10^\circ$ and $a_c = 0.2$ mm; (d) $\gamma = 20^\circ$ and $a_c = 0.2$ mm [17].....	22
Figure 2.9: Schematic view of sub-models and chip formation mechanisms in each of the four fibre orientation intervals [19].....	23
Figure 2.10: Schematic view of (a) Exemplary new (blue) and worn (green) cutting edge profile and (b) evaluation of current micro geometry with five micro-geometry parameters [19]	24
Figure 2.11: Cross-section of 'quick-stop' specimens showing the notch formed by the tool: (a) machined perpendicular to the fibers; (b) machined parallel to the fibers [20]	26
Figure 2.12: Cutting mechanisms in the orthogonal machining [21].....	27
Figure 2.13: Deformation mechanisms based on depth of cut [22].....	28
Figure 2.14: The finite element model with (a) Tool geometry; (b) Boundary conditions and cutting forces [23].....	29
Figure 2.15: Comparison between experimental cutting forces and simulations, 0.120 mm depth of cut, 10° rake angle, 17° clearance angle: (a) Principal cutting force; (b) Thrust force [23]	30
Figure 2.16: Cutting forces versus fiber orientation for anisotropic EHM [24]	31
Figure 2.17: Comparison between experimental cutting forces and simulations: (a) Principal cutting force; (b) Thrust force [26].....	32

Figure 2.18: Finite element model of a single fiber with surrounded matrix; (a) 30° fiber orientation, (b) 90° fiber orientation [27].....	33
Figure 2.19: Comparison between experimental cutting forces and simulations: (a) Principal cutting force; (b) Thrust force [27].....	33
Figure 2.20: (a) Schematic view of fiber, matrix and EHM zones used in finite element modeling; (b) 25 fiber, 26 matrix and 2 EHM layers used in finite element model [28].....	35
Figure 2.21: Simulation results with (a) 45° and 90° failure nodes; (b) 45° , 15 μm depth of cut; (c) 45° , 30 μm depth of cut; (d) 90° , 15 μm depth of cut; (e) 90° , 30 μm depth of cut [29]	36
Figure 2.22: Illustration of (a) EVA cutting of FRP composite and (b) its FE micro-scale model [30]	37
Figure 2.23: (a) Cutting Force and (b) thrust force comparison for Novel Approach and Approach 3 against experimental results [32].....	38
Figure 3.1: (a) Schematic illustration of sequential cutting on a UD-CFRP composite, (b) the microstructure-based FE model for cutting UD-CFRP.....	43
Figure 3.2: The traction-separation response of interface under normal loading.....	47
Figure 4.1: Experimental setup for oblique cutting of UD-CFRP.....	49
Figure 4.2: (a) Carbide turning inserts and (b) Tool holder.....	50
Figure 4.3: Kistler 9257B dynamometer to capture cutting forces.....	51
Figure 4.4: Severe bulk damage on the CFRP part when cutting with 135° fiber orientation angle.....	52
Figure 4.5: Simulated chip formation in steady state cutting for: (a) $\theta= 0^\circ, i= 0^\circ$, (b) $\theta=0^\circ, i= 60^\circ$	53

Figure 4.6: Experimental chip formation in steady state cutting for $\theta=0^\circ$ and: (a) $i= 0^\circ$, (b) $i= 15^\circ$, (c) $i= 30^\circ$, (d) $i= 45^\circ$, (e) $i= 60^\circ$	54
Figure 4.7: Simulated chip formation in steady state cutting for: (a) $\theta= 45^\circ$, $i= 0^\circ$, (b) $\theta=45^\circ$, $i= 30^\circ$	55
Figure 4.8: Experimental chip formation in steady state cutting for $\theta=45^\circ$ and: (a) $i= 0^\circ$, (b) $i= 15^\circ$, (c) $i= 30^\circ$, (d) $i= 45^\circ$, (e) $i= 60^\circ$	56
Figure 4.9: Simulated chip formation in steady state cutting for: (a) $\theta=90^\circ$, $i= 0^\circ$, (b) $\theta=90^\circ$, $i= 30^\circ$	57
Figure 4.10: Experimental chip formation in steady state cutting for $\theta=90^\circ$ and: (a) $i= 0^\circ$, (b) $i= 15^\circ$, (c) $i= 30^\circ$, (d) $i= 45^\circ$, (e) $i= 60^\circ$	58
Figure 4.11: Cutting forces of fiber orientation $\theta=45^\circ$ and tool inclination angle $i= 30^\circ$ in simulation.....	60
Figure 4.12: Cutting forces of fiber orientation $\theta= 0^\circ$ and tool inclination angle $i= 30^\circ$ in experiment.....	60
Figure 4.13: Comparison between simulated and experimental forces with fiber orientation $\theta = 0^\circ$	62
Figure 4.14: Comparison between simulated and experimental forces with fiber orientation $\theta = 45^\circ$	63
Figure 4.15: Comparison between simulated and experimental forces with fiber orientation $\theta = 90^\circ$	64
Figure 5.1: Simulation results of the machined surface for (a) $\theta= 0^\circ$, $i= 0^\circ$, (b) $\theta= 0^\circ$, $i= 30^\circ$, (c) $\theta= 0^\circ$, $i= 45^\circ$	66

Figure 5.2: Simulation results of the machined surface for (a) $\theta= 45^\circ, i= 0^\circ$, (b) $\theta= 45^\circ, i= 45^\circ$, (c) $\theta= 45^\circ, i= 60^\circ$67

Figure 5.3: Simulation result of the finished surface microstructure for the cutting with (a) $\theta= 90^\circ, i= 0^\circ$, (b) $\theta= 90^\circ, i= 30^\circ$, (c) $\theta= 90^\circ, i= 45^\circ$69

Figure 5.4: Simulation results of the subsurface damage for: (a) $\theta= 0^\circ$, first cut, (b) $\theta= 0^\circ$, second cut, (c) $\theta= 45^\circ$, first cut, (d) $\theta=45^\circ$, second cut, (e) $\theta=90^\circ$, first cut, (f) $\theta=90^\circ$, second cut.....71

Figure 5.5: Comparison of cutting forces between the first and the second cuts with fiber orientation angle: (a) $\theta= 0^\circ$, (b) $\theta= 45^\circ$, (c) $\theta= 90^\circ$. F_c represents the tangential force; F_r represents the out-of-plane force.....72

Figure 5.6: Simulation results of the subsurface damage depth at different fiber orientation angles.....73

Figure 5.7: Schematic illustration of (a) workpiece with uniform distributed fibers, (b) workpiece with random distributed fibers.....74

List of Symbols

α :	Rake angle of the tool
β :	Friction angle
γ :	Clearance angle of the tool
i :	Oblique angle
η :	Chip-flow angle
r :	Tool edge radius
θ :	Fiber orientation angle
D :	Diameter of the fiber
v :	Cutting speed / Poisson's ratio
h :	Uncut chip thickness
X_T :	Tensile strength in longitudinal direction
X_C :	Compressive strength in longitudinal direction
Y_T :	Tensile strength in transverse direction
Y_C :	Compressive strength in transverse direction
σ_{ii} :	Stress tensor component of the fiber
E :	Elasticity modulus
G :	Shear modulus
D :	Stiffness degradation factor
t :	Nominal traction stress vector

σ_y :	Yield strength
σ_{\max} :	Normal strength
τ_{\max} :	Shear strength
K_{nn}, K_{ss}, K_{tt} :	Elastic stiffness in three directions
G_C :	Fracture energy
F_c :	Cutting force in tangential directions out-of-plane
F_r :	Cutting force in out-of-plane directions

List of Abbreviations

CFRP:	Carbon Fiber Reinforced Polymer
CNC:	Computer Numerical Control
EHM:	Equivalent Homogenous Material
EVA:	Elliptic Vibration-Assisted
FE:	Finite Element
FEM:	Finite Element Method
FRP:	Fiber Reinforced Polymer
GFRP:	Glass Fiber Reinforced Polymer
MPEP:	Minimum Potential Energy Principle
RVE:	Representative Volume Element
SEM:	Scanning Electron Microscope
UD-CFRP:	Uni- Directional Carbon Fiber Reinforced Polymer
UD-FRP:	Uni- Directional Fiber Reinforced Polymer
UD-GFRP:	Uni- Directional Glass Fiber Reinforced Polymer

Acknowledgements

First of all, this thesis will not be possible without the generous support from my supervisor Dr. Xiaoliang Jin. He encouraged me to explore my research interest from the very start of the graduate school and guided me throughout both the research and writing stages. Without his academic supervision and emotional guidance, I would not acquire the skills mastering both the simulations and experiments of this thesis.

I would also extend my gratitude to my lab mates in the past two years. They taught me what a qualified scholar of mechanical engineering should be and supported my research with their unique insights. Bingxun Li, Naresh Kumar Maroju and Wenshuo Ma helped me polish the skills in both research conducting and thesis writing. I am also grateful to my fellow graduate students: Dr. Shaoke Wan and Chunlei Song. They accompanied me over these years and made Vancouver home to me.

My deepest appreciation goes to my dear parents for allowing their only child to travel to the opposite side of the world to pursue a master's degree. It is their support that allows me to focus on my dream without any hesitation.

Last but not the least, I must express my deep love and gratitude to my wife, Elina Jin, for encouraging and supporting me throughout my master's life. Her encouragement is not only in present work, but also in every aspect in my life.

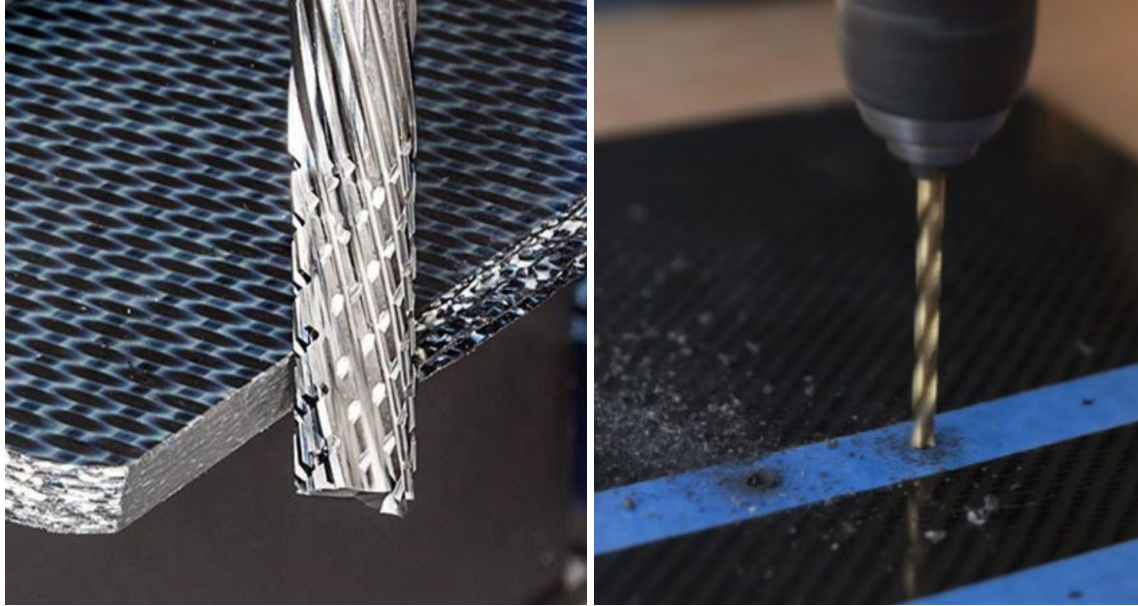
This research is sponsored by Natural Sciences and Engineering Research Council of Canada (NSERC) - Collaborative Research and Development (CRD) grant (530095 - 18).

Chapter 1: Introduction

1.1 Background

Carbon Fiber Reinforced Polymer Composites (CFRP) are lightweight, high strength materials made of a polymer matrix reinforced with carbon fibers. CFRP composites have been used in aerospace, aviation, and automotive industries due to their high strength-to-weight ratio, high temperature and corrosion resistance. However, one major factor which limits the industrial applications of CFRP is the high cost. Compared to certain metal alloys such as steel or aluminum, the price of CFRP composites can be anywhere between 5 times to 100 times more expensive. This is partially because of the high manufacturing costs of CFRP composites.

CFRP parts are usually produced in near net-shape. Cutting operations (e.g. drilling, slot milling and edge trimming) are required to remove excessive materials in order to fulfill the assembly, geometry, and surface quality requirements of the final CFRP components. Some typical machining operations of CFRP are shown in Fig 1.1. Due to the two-constituent (fiber reinforcement and matrix) structure and anisotropic property of CFRP, the cutting mechanism is completely different compared to that in cutting of metal alloys. The cutting process involves fiber breakage, matrix cracking, and fiber-matrix debonding. If the cutting tool geometry or process parameters are not selected properly, the cutting operation will lead to subsurface damage, burrs formation, fiber pull-out, and delamination, which result in part damage and low manufacturing process efficiency. Fig 1.2 shows the typical damages caused by cutting processes.



(a)

(b)

Fig. 1.1. (a) Edge trimming and (b) drilling operations of CFRP.



(a)

(b)

(c)

Fig. 1.2. Delamination and burrs in (a) drilling [1], (b) milling [1] and (c) oblique cutting process.

The mechanics of cutting CFRP composites has been studied in order to enhance the cutting process performance and reduce the costs of CFRP components. There are three major methods for investigating the cutting mechanics of CFRP: analytical modeling, experimental investigation

and numerical simulation. Because of the inhomogeneous and anisotropic nature of CFRP composite, different analytical models must be established respectively for different ranges of fiber orientation angles. Experimental investigations are expensive and time consuming, and the results are only applicable within the tested ranges of cutting parameters in the experiments. Moreover, in most of the cutting conditions, the chips are in the form of powder, which may cause potential harm to the health of the machine operators.

With the development of finite element method (FEM) and computational capability, numerical simulation has become a promising technique to study cutting mechanics of CFRP. Moreover, FE simulation is able to simulate the cutting process with various cutting parameters, including uncut chip thickness, cutting speed, fiber orientation, as well as cutting tool geometry parameters such as rake angle, clearance angle, and tool edge radius, with much lower cost than experimental method. Nevertheless, a trade-off must be considered between the computational cost and the prediction accuracy when implementing the numerical simulations.

1.2 Structure of carbon fiber reinforced polymer

1.2.1 Carbon fiber

Carbon fibers are the constituent material that provide the strength to CFRP composites and take most of the loading. Different length or directions of carbon fibers will change the properties of the CFRP composite significantly. Carbon fibers may be continuous, discontinuous, or particles staggered through the matrix material (Fig. 1.3). Continuous fibers usually have one long axis with very small diameter varying from 5-20 μm . At the atomic level, carbon fiber is very similar to

graphite and is composed of layers of carbon atoms arranged in a hexagonal pattern (graphene flakes). The difference between carbon fibers and graphite lies in the way the layers are connected. Graphite is a crystalline structure, and its interlayer connections are loose, while carbon fiber is not a crystalline structure, and the interlayer connections are irregular. This structure prevents slippage and enhances material strength.

Carbon fibers are transversely isotropic material [2] and have significantly higher strength and stiffness along the axial than in the transverse direction. This property limits the application of CFRP composites in areas that requires high strength and stiffness in all directions. Another property that limits their use is the very high electric conductivity. In most of the cutting conditions, the chips are in the form of powder, which may cause short circuit of the electric instruments if they are not properly collected.

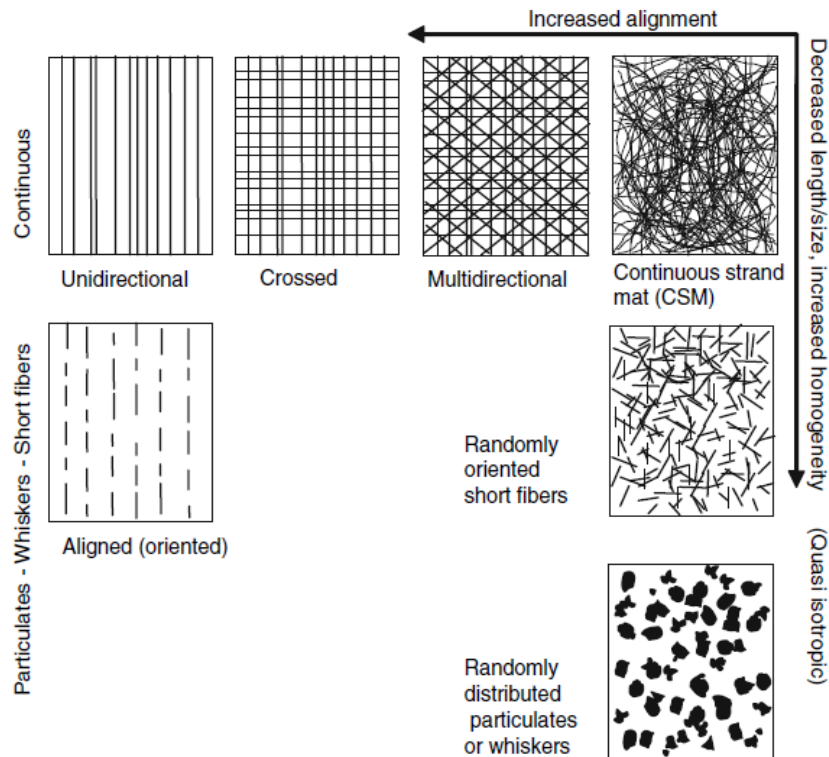


Fig.1.3. Schematic of different reinforcement arrangements in composites [3].

1.2.2 Matrix

The matrix is used to bind the fibers in order to provide the shape of composites, transfer the loads between fibers and matrix and protect fibers from abrasion. Matrix material could be metals, ceramics, or polymers. In CFRP composite, polymer matrix is used, which are in the form of either thermoplastics or thermosets. Thermosetting polymer (also known as thermosetting plastic) refers to polymer that may not be softened and reheated again. When heated to a certain temperature, cross-linking solidifies and becomes hard, and this change is irreversible. The molecular chains of thermosetting polymers are linear or branched before curing. After curing, chemical bonds are formed between the molecular chains to form a three-dimensional network structure, therefore, they can neither be melted again nor be dissolved in solvents. Commonly used thermosetting plastics are phenolic resin, urea-formaldehyde resin, melamine resin, unsaturated polyester resin, epoxy resin, silicone resin, polyurethane etc. Most thermosetting polymers have better mechanical properties and higher working temperature with lower cost at the same time compared to thermoplastic.

Thermoplastics refer to plastics that have the characteristics of softening when heated and hardening when cooled. This process is reversible and can be repeated. Commonly used thermoplastics are polyethylene, polypropylene, polyvinyl chloride, polystyrene, polyoxymethylene, polycarbonate, polyamide, acrylic plastics etc. The molecular chains of resins in thermoplastics are linear or branched structures. No chemical bond is generated between the molecular chains.

1.3 Machining of CFRP

In this section, the characteristics of machining CFRP due to its two-constituent structure and the mechanical properties of fiber and matrix materials is summarized. In actual machining operations such as slot milling and edge trimming, the material removal is in the form of oblique cutting. The comparison of configurations between orthogonal and oblique cutting is presented, followed by introducing the significance of oblique cutting in milling of CFRP.

1.3.1 Characteristics of machining CFRP

The main characteristics of machining CFRP are described below:

- (1) CFRP material is a multi-phase material with a layered graphite structure. The machining process involves fiber breakage, matrix cracking, and fiber-matrix debonding. If the cutting tool geometry or process parameters are not selected properly, the machining operation will lead to subsurface damage, fiber pull-out and delamination.
- (2) CFRP is a typical inhomogeneous and anisotropic material, and its mechanical properties vary significantly in different directions. Therefore, when machining CFRP materials, in order to prevent the occurrence of delamination and splitting of the workpiece, the effect of the fiber orientation on the cutting mechanics has to be understood.
- (3) Due to the brittleness of carbon fiber, the chips produced by CFRP machining process are usually powder-like, which is completely different from the continuous chip formation in metal cutting, as shown in Fig.1.4 and Fig.1.5. This is one of the major differences in analyzing the cutting mechanics for CFRP and metal alloys.

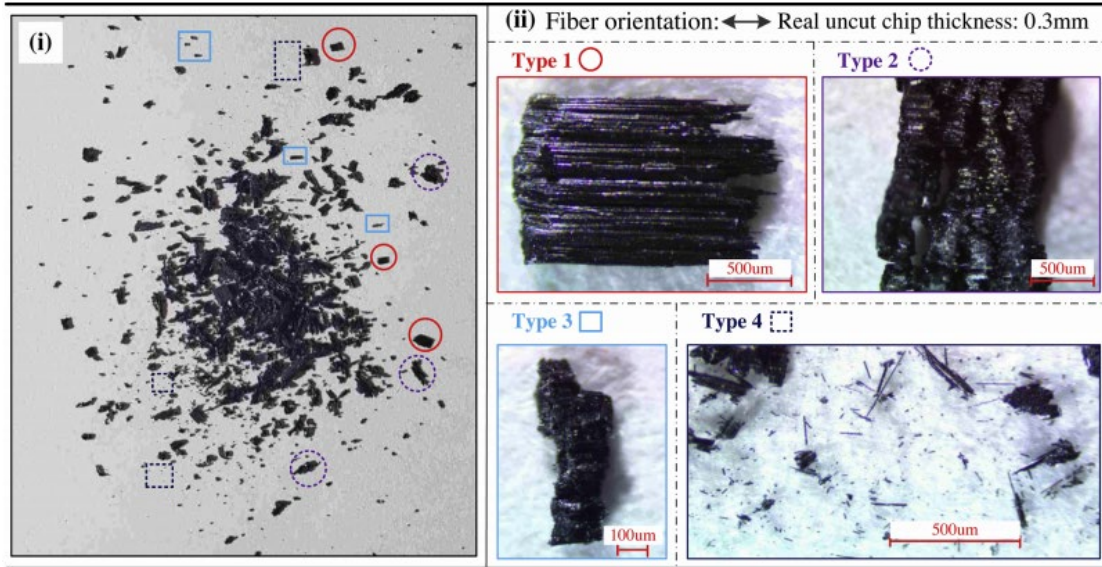


Fig.1.4. Typical powder-like chips formed in orthogonal cutting experiment [4].

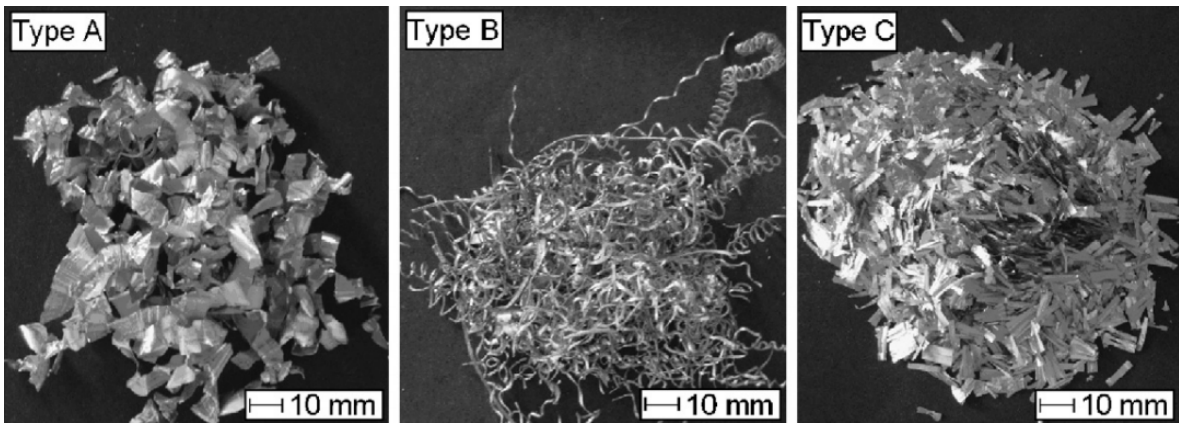


Fig.1.5. Typical aluminum chips formed in milling process [5].

1.3.2 Orthogonal and oblique cutting

In orthogonal cutting process, the cutting tool edge is perpendicular to the direction of tool motion, as shown in Fig. 1.6(a). The material deformation is generally assumed to occur in a 2-D plane perpendicular to tool edge by applying plane-strain condition. Therefore, the cutting force

components only within the 2-D plane are considered. However, in oblique cutting, the cutting tool edge is not perpendicular to the cutting velocity direction, as shown in Fig. 1.6(b). A non-zero inclination angle (i) is used to define the oblique angle. As a result, the material deformation also occurs in the out-of-plane direction, and cutting forces are generated in all three directions. The oblique angle significantly influences the chip formation, cutting force, and surface generation in machining of CFRP.

For mechanics of oblique cutting of metal alloys, Stabler's theory [6] is used, i.e. the chip-flow angle (η) is assumed to be equal to the cutting tool inclination angle (i). However, the Stabler's theory cannot be directly used for CFRP, because the machined chips in machining CFRP are mostly in the form of powders, and the chip morphology highly depends on the fiber orientation angle, which is not the case in metal cutting.

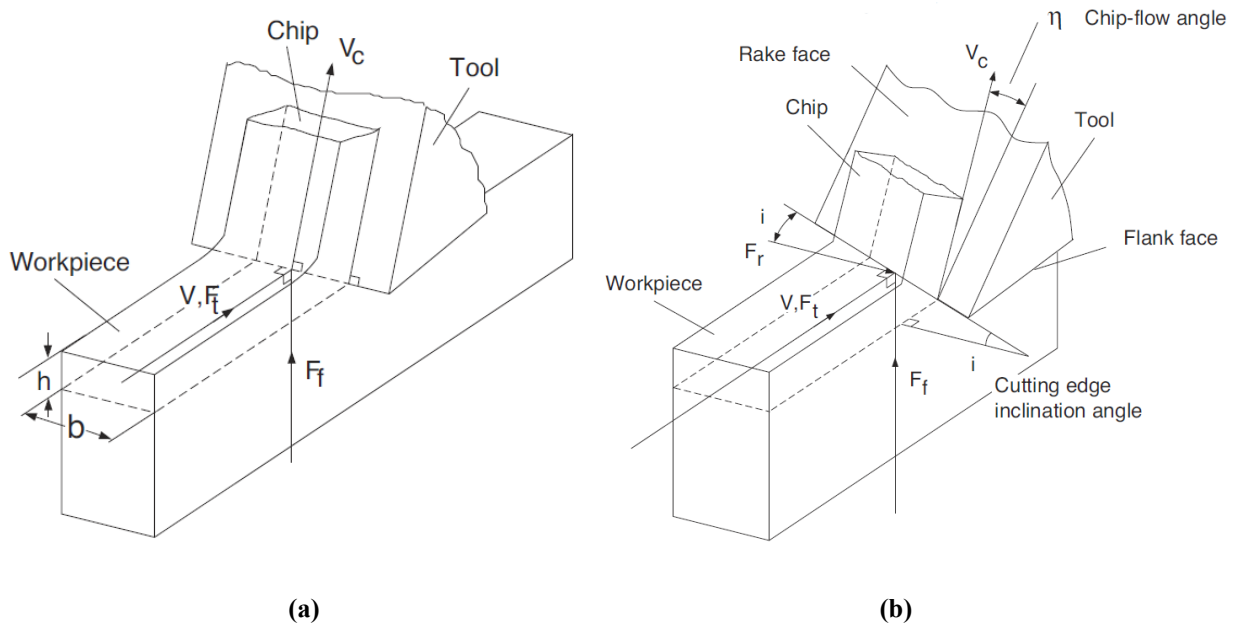


Fig. 1.6. Schematic illustration of (a) orthogonal cutting and (b) oblique cutting [7].

1.3.3 Milling of CFRP

Milling is one of the most common machining operations for slotting and edge trimming of CFRP components. A schematic of milling process of CFRP is shown in Fig. 1.7 (a). The material removal in milling can be considered as the combination of the oblique cutting at the cutting edge, as shown in Fig. 1.7 (b). The fiber orientation angle (θ) is defined by the fiber direction and cutting direction. The inclination angle is equal to the helix angle of the milling tool. Due to the helix angle, a vertical force (F_z in Fig. 1.7 (a)) is generated along the interlaminar direction, and can cause delamination of the CFRP components.

The helix angle of milling tool usually varies between 0° and 60° . Higher helix angle can be used with higher cutting speeds and feeds, resulting in higher material removal rate. Increasing the helix angle in metal cutting can also reduce the tool deflection by transferring stress vertically through the spindle. However, high helix angle corresponds to large oblique angle at the cutting tool edge, which can cause chip formation in the out-of-plane direction, CFRP delamination and subsurface damage. Therefore, proper helix angle design is essential in optimization of tool design and process planning for machining CFRP. Thus, research on oblique cutting is necessary in order to understand the cutting mechanics of CFRP, and enhance the performance in practical machining of CFRP components.

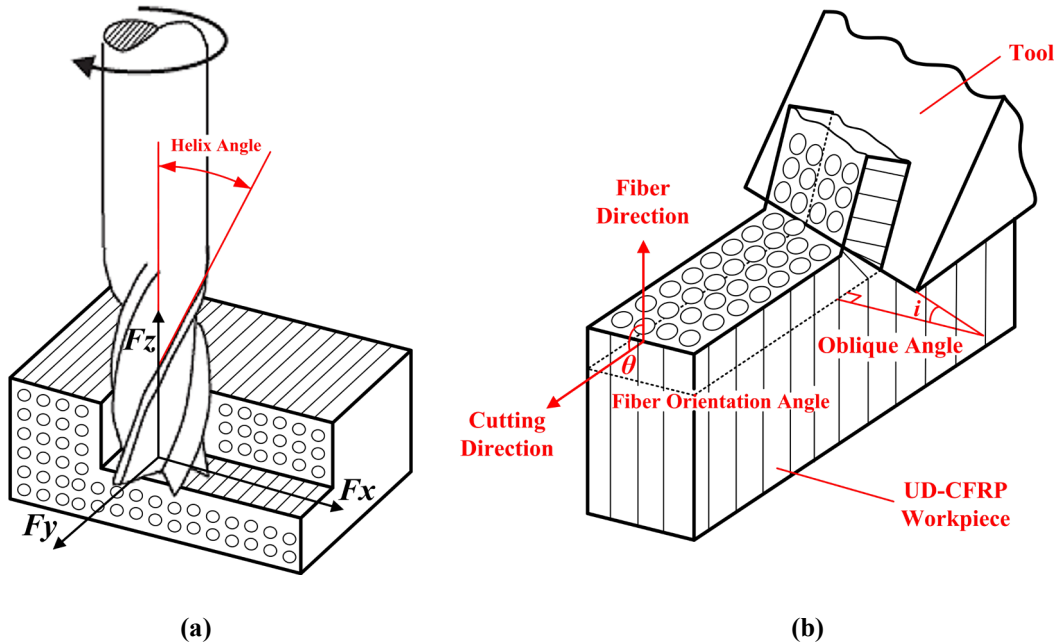


Fig. 1.7. (a) Milling process of CFRP and helix angle definition and (b) oblique cutting of UD-CFRP.

1.4 Research objective

The oblique angle plays a significant role in the chip formation, cutting force generation and subsurface damage in actual machining of CFRP, and this cannot be analyzed from mechanics model of 2-D orthogonal cutting. Furthermore, the commonly used Stabler's theory [6] for modeling oblique cutting of metal alloys cannot be directly used for CFRP because of the powder type and fiber orientation dependent chip formation. Therefore, the first objective of this thesis is to determine the effect of oblique angle and fiber orientation angle on out-of-plane chip formation, cutting force, and surface generation in oblique cutting of CFRP.

Moreover, actual machining operation involves multiple tooth passing. Therefore, machining is always performed on the material with existing damage and residual stresses due to previous cutting processes, defined as sequential cutting, as shown in Fig.1.8. In this thesis, the sequential

cutting process is modeled and simulated considering the effect of the cutting induced subsurface damage on force and surface generation in subsequent cutting process.

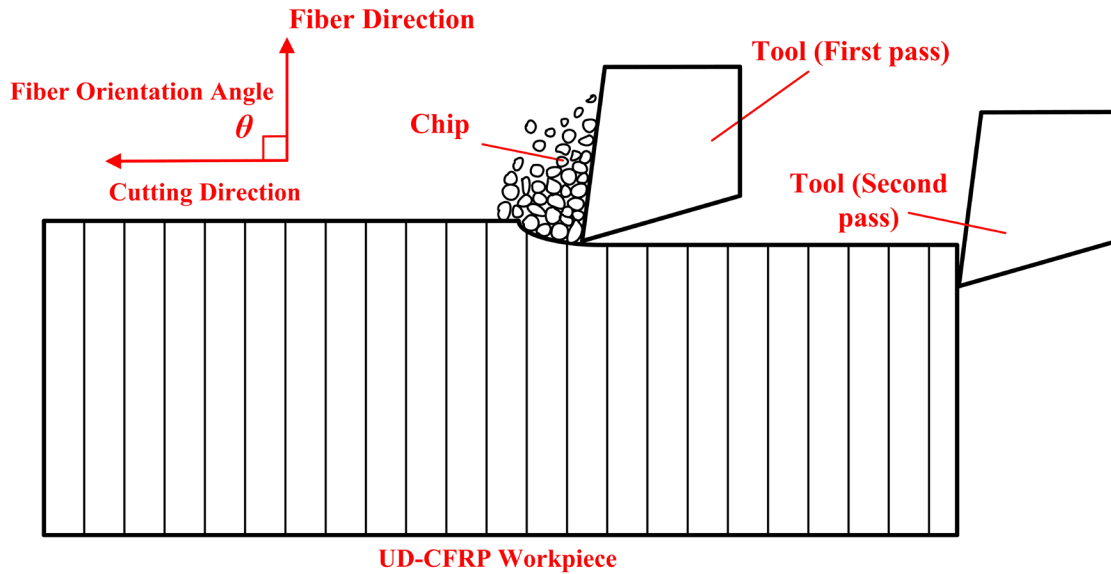


Fig. 1.8. Sequential cutting of UD-CFRP workpiece.

To my knowledge, there has been no numerical model on oblique or sequential cutting of CFRP. The results of this thesis will address this gap and to reflect the condition in actual cutting operation. This thesis develops a new three-dimensional (3-D) model of oblique cutting of UD-CFRP considering the mechanical properties of fiber, matrix, and interface individually. The effects of oblique angle and fiber orientation angle on the chip formation, cutting force generation, and surface generation in oblique cutting of CFRP are simulated and analyzed. Oblique cutting experiments are conducted to evaluate the model by comparing the chip morphology and cutting force values. The subsequent sections are organized as follows: Chapter 2 presents the literature review. Chapter 3 presents the finite element model and material modeling. Chapter 4 shows the simulation results with experimental comparison on chip morphology and cutting forces. Chapter 5 includes detailed analyses and discussions, and the conclusion is presented in Chapter 6.

Chapter 2: Literature review

In the literature, the purpose of studying the cutting mechanics of FRP composites is to understand the mechanisms of chip formation and surface generation in machining FRP composites, and predict the cutting forces based on given tool geometries and cutting conditions. The results will provide guidance for the process planning, in order to improve the machining efficiency and part quality in machining FRP composites, there are three major methods in studying the mechanics of cutting CFRP: analytical mechanics model, experimental investigation, and numerical simulation. The literature work in these three categories are reviewed in the following sections.

2.1 Analytical studies

2.1.1 Macro-mechanical analytical models

Analytical mechanics models of cutting CFRP have been developed to understand the material removal mechanism in order to enhance the cutting performance. Macro-mechanical models assume the inhomogeneous FRP composites as their equivalent continuous homogeneous materials (EHM) in order to simplify the modeling and analysis. The EHM model of the CFRP is based on the mechanical property of the constituents and the volume fraction of the fiber. Everstine and Rogers [8] are the first group working on modeling the machining of FRP composites. They developed an analytical force model based on thick shear plane theory, which is only applicable for parallel fiber orientation, i.e. 0° fiber orientation angle. The schematic diagram

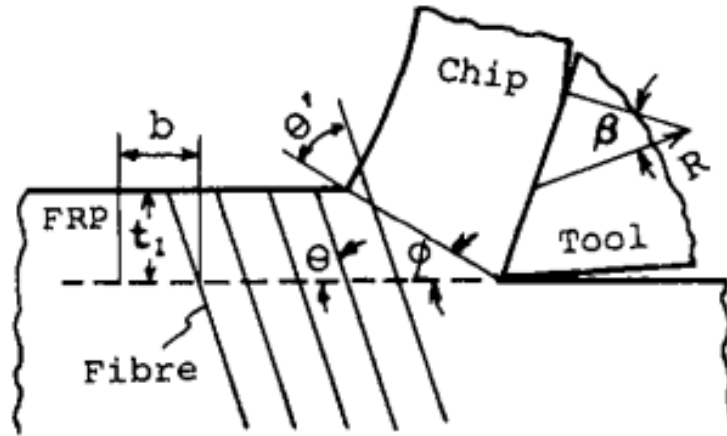


Fig. 2.2. Orthogonal cutting model of FRP from Takeyama and Iijima [9].

The mechanistic model of metal cutting is used to predict the principal and thrust forces, expressed as:

$$F_c = \frac{bt_d\tau(\theta')\cos(\beta-\gamma)}{\cos(\phi+\beta-\gamma)\sin(\phi)}$$

$$F_t = \frac{bt_d\tau(\theta')\sin(\beta-\gamma)}{\cos(\phi+\beta-\gamma)\sin(\phi)}$$
(2.2)

where ϕ is the shear angle, θ is the fiber orientation and θ' is the shear fiber angle, i.e. the angle between shear plane and fiber orientation. $\tau(\theta')$ is the yield stress of GFRP, t_d is uncut chip thickness, γ and β are the rake angle of and friction angle, respectively.

The comparison of the experimental and the predicted cutting force results is illustrated in Fig. 2.3. It is shown that the model is able to predict the forces with acceptable accuracy in the fiber orientation between 0° and 60° . Moreover, it should be noted that unlike metal cutting in which the chips are formed continuously, the chips in machining of FRP are in the form of powder for most of the cutting conditions. Therefore, it is difficult to determine the shear plane angle, which requires the measurement of the chip thickness.

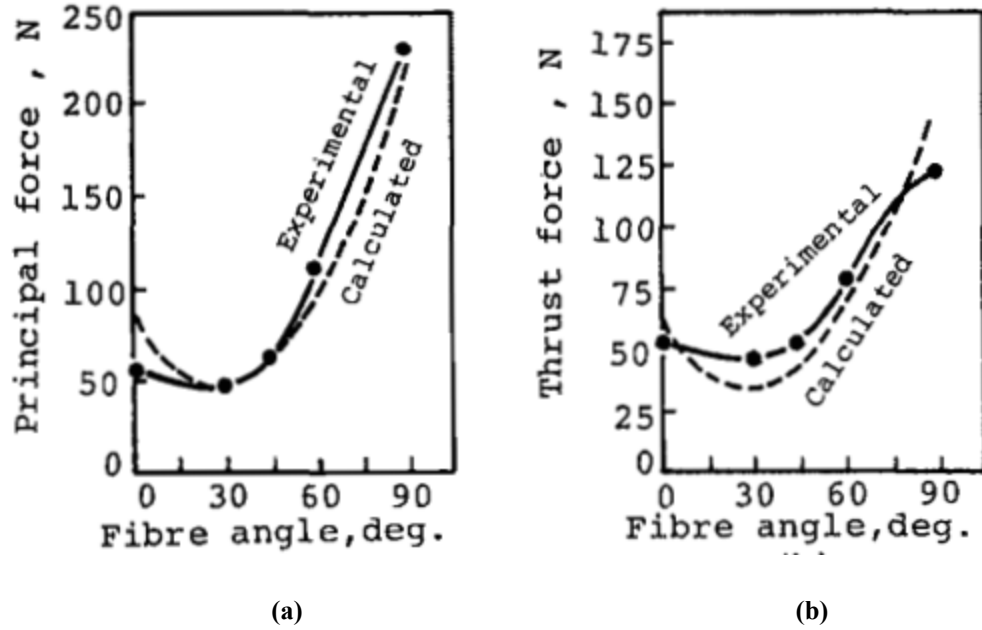


Fig. 2.3. Comparison of experimental and calculated data for (a) principal and (b) thrust force from Takeyama and Iijima [9] model.

For fiber orientation angle larger than 90° , Bhatnagar et al. [10] proposed an analytical force model assuming that the shear plane angle always equals to the fiber orientation angle. Therefore, they overcome the difficulty of identifying the shear plane angle in the model by Takayama and Iijima [9]. The principal and thrust forces are therefore expressed by:

$$\begin{aligned}
 F_c &= \tau_0 A_0 \frac{\cos(\beta_m - \gamma)}{\sin \theta \cos(\theta + \beta_m - \gamma)} \\
 F_t &= \tau_0 A_0 \frac{\sin(\beta_m - \gamma)}{\sin \theta \cos(\theta + \beta_m - \gamma)}
 \end{aligned}
 \tag{2.3}$$

where A_0 is the area of undeformed chip, τ_0 is the shear strength, β_m is the mean friction angle.

However, the assumption of shear angle equaling to fiber orientation angle is not validated.

Zhang et al. [11] predicted the forces in orthogonal cutting of UD-CFRP when fiber orientation angle is between 0° and 90°. They divided the cutting edge geometry into three parts: rake face, cutting edge and flank face, which correspond to chipping Region 1, pressing Region 2 and bouncing Region 3, as shown in Fig. 2.4.

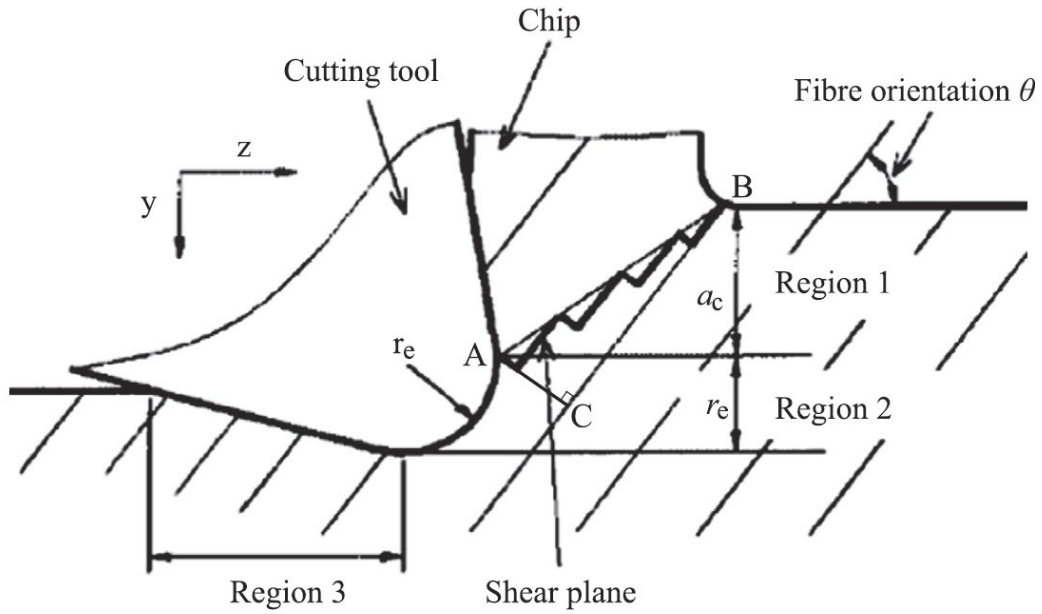


Fig. 2.4. Definitions of the deformation zones [11].

In Region 1, based on the classical Merchant's thin shear plane theory for metal cutting, forces in y and z directions are expressed as:

$$\begin{aligned}
 F_{y1} &= \tau_1 h_0 a_c \frac{\cos \phi \tan(\phi + \beta - \gamma) - \sin \phi}{\frac{\tau_1}{\tau_2} \cos(\theta - \phi) \sin \theta - \sin(\theta - \phi) \cos \theta} \\
 F_{z1} &= \tau_1 h_0 a_c \frac{\sin \phi \tan(\phi + \beta - \gamma) + \cos \phi}{\frac{\tau_1}{\tau_2} \cos(\theta - \phi) \sin \theta - \sin(\theta - \phi) \cos \theta}
 \end{aligned} \tag{2.4}$$

where τ_1 and τ_2 are the shear strengths of FRP composite perpendicular to and along fiber directions. β is the friction angle on the rake face. h_0 is the thickness of the workpiece and a_c is the actual depth of cut.

Based on the indentation mechanics of a circular cylinder in contact with a half-space [11,12], the forces in Region 2 (close to the round tool edge) are expressed by:

$$\begin{aligned} F_{y2} &= P_{\text{real}}(\cos \theta - \mu \sin \theta) \\ F_{z2} &= P_{\text{real}}(\sin \theta + \mu \cos \theta) \end{aligned} \quad (2.5)$$

where P_{real} is the real resultant force in region 2.

Based on the contact mechanics between a wedge and a half-space [11,13], the forces in Region 3 (at the tool flank face) are expressed by:

$$\begin{aligned} F_{y3} &= \frac{1}{2} r_e E_3 h_0 (1 - \mu \cos \alpha \sin \alpha) \\ F_{z3} &= \frac{1}{2} r_e E_3 h_0 \cos^2 \alpha \end{aligned} \quad (2.6)$$

where r_e is the edge radius, α is the clearance angle of the tool, and E_3 is the effective modulus of the FRP composite in Region 3.

Cutting forces were calculated by adding individual force component from each of these three regions, therefore, the tool-workpiece interaction at the tool edge and flank face is considered. Comparisons between the predicted and experimental measurements is shown in Fig. 2.5, which demonstrates the prediction accuracy of the proposed model

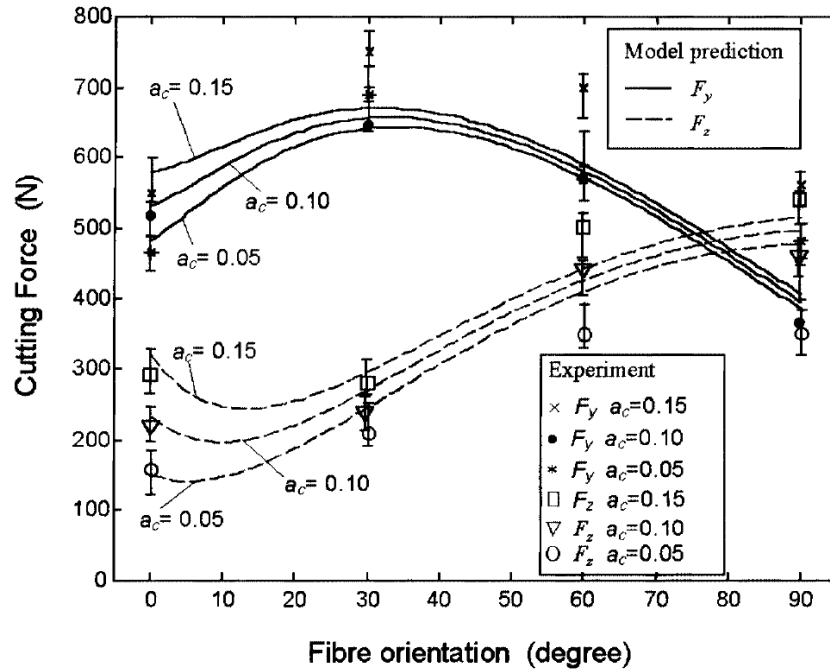


Fig. 2.5. Comparison between model predictions and experimental measurements [11].

Although the analytical mechanics model is able to predict the cutting force, it does not present the detailed chip formation and surface generation, because the model does not consider the fiber, matrix and interface respectively. Furthermore, the shear angle value is based on assumptions without systematic validation.

2.1.2 Micro-mechanical analytical models

Due to the inhomogeneous and anisotropic property of FRP, the material removal in machining is in the form of fiber bending, bucking, or matrix shearing, depending on the fiber orientation and tool geometry. This is completely different from metal cutting, in which the material removal is achieved through shearing in the primary shear plane in front of the tool edge. In micro-scale

where E_m and E_f are the transverse Young's modulus of EHM and fiber; ν_m is the Poisson's ratio of EHM. The model considers the effects of the fiber deformation, fiber fracture and fiber–matrix debonding. The results show that the cutting forces, the extent of fiber deformation and fiber–matrix debonding reduce with the application of tool vibration assistance, which results in better surface finish. However, the model is only applicable to 90° fiber orientation angle, and it focuses on the deformation of a single fiber rather than whole deformation zone.

Qi et al. [17] established an analytical force model of UD-CFRP orthogonal cutting, focusing on the deflection of the representative volume element (RVE) including a single fiber and the surrounding matrix. They divided the cutting zone into three areas: cutting tool tip, flank face and rake face (see Fig. 2.7. (a)), which correspond to areas A , B and C . Cutting force were calculated by adding single forces acting on each of these three areas, which can be expressed by:

$$\begin{aligned} F_x &= \frac{b}{2r_m} (F_{Ax} + F_{Cx} + F_{Bx}) \\ F_y &= \frac{b}{2r_m} (F_{Ay} + F_{Cy} + F_{By}) \end{aligned} \quad (2.8)$$

where F_{Ax} , F_{Bx} and F_{Cx} correspond to the forces in x- direction, and F_{Ay} , F_{By} and F_{Cy} are the forces in y direction in the areas A , B and C . r_m is the radius of the RVE, b is the cutting width. The fiber bending in area A is modeled based on the minimum potential energy principle (MPEP) and Winkler's foundation theory [18] to the REV. Theoretical model shows that the fiber orientation, cutting depth and rake angle can influence the cutting and thrust forces significantly.

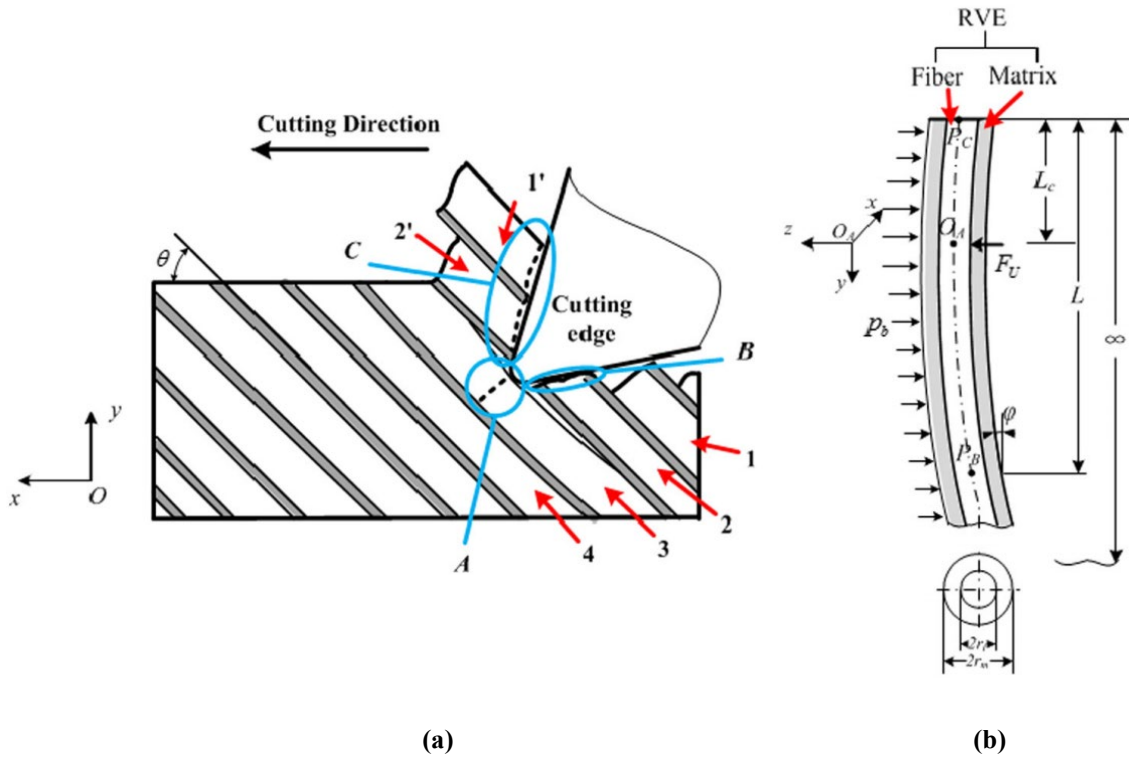


Fig. 2.7. (a) Three regions in orthogonal cutting; (b) Load condition of RVE [17].

The predicted forces agreed well with the experimental results, as shown in Fig. 2.8. However, their model can only be used for fiber orientation ranging from 0° to $90^\circ + \gamma$, where γ is the rake angle of the cutting tool.

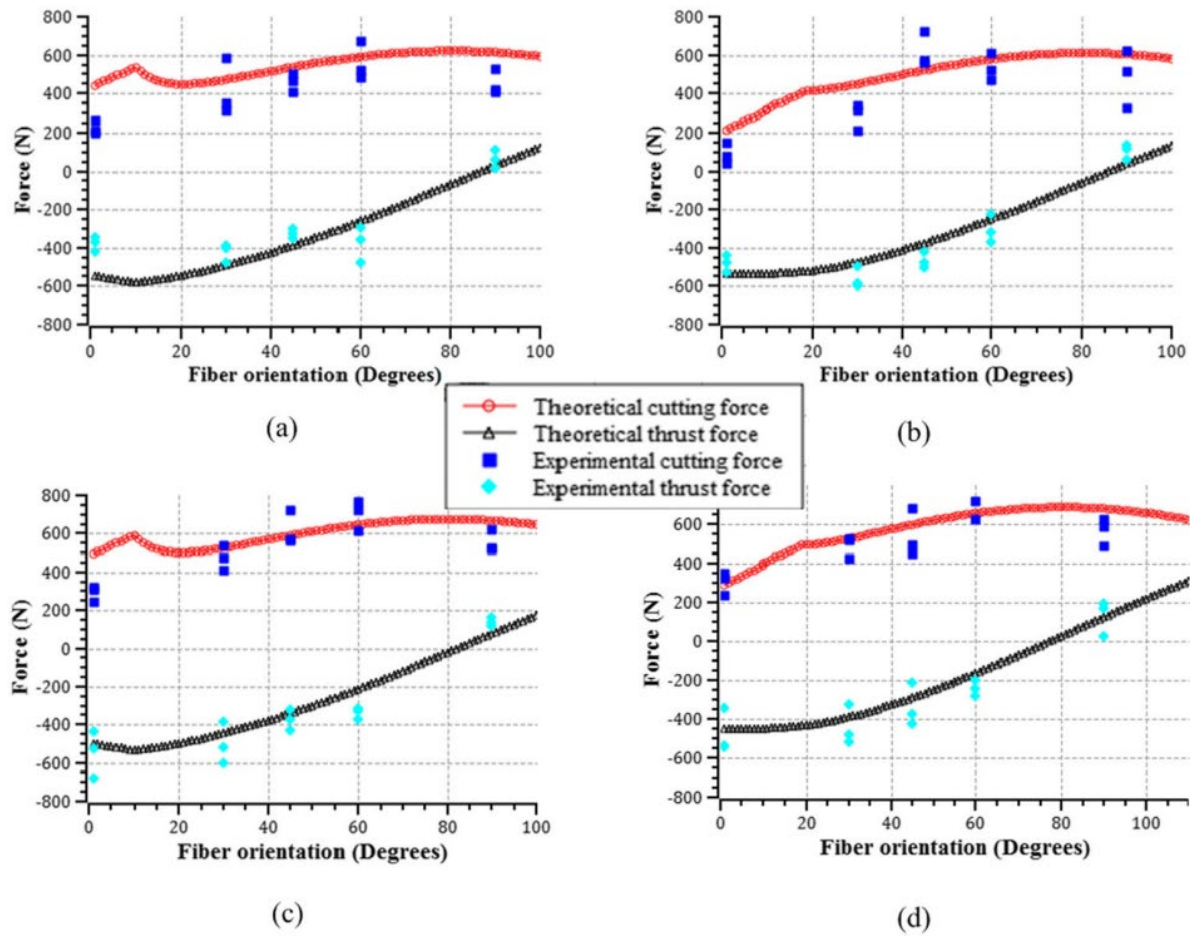


Fig. 2.8. Theoretical and experimental cutting and thrust forces versus fiber orientation with: (a) $\gamma = 10^\circ$ and $a_c = 0.1$ mm; (b) $\gamma = 20^\circ$ and $a_c = 0.1$ mm; (c) $\gamma = 10^\circ$ and $a_c = 0.2$ mm; (d) $\gamma = 20^\circ$ and $a_c = 0.2$ mm [17].

Voss, et al. [19] proposed an analytical force model for orthogonal UD-CFRP cutting which considers the effect of fiber orientation angle and tool flank wear. The entire range of fiber orientation (0° to 180°) is divided into four ranges, with each range corresponding to a specific sub-model. In their model, the cutting region is divided into three sub-regions, as suggested by

Zhang et al. [11]. The schematic view of each separate sub-model and chip formation mechanisms in each of the four fibre orientation ranges are shown in Fig. 2.9.

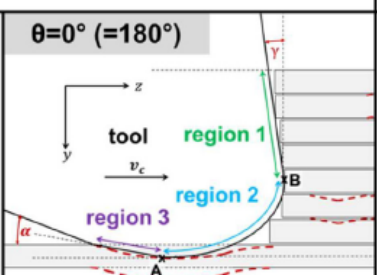
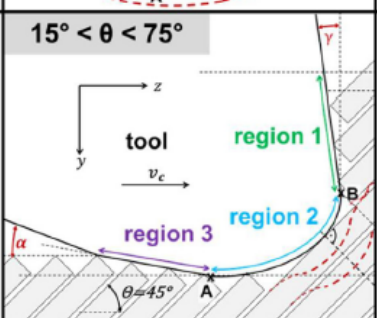
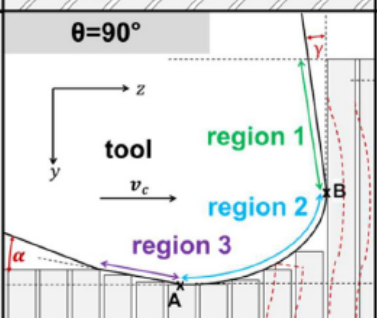
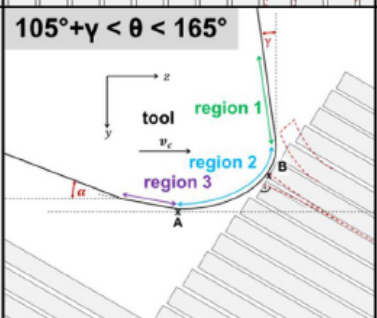
		Region 1	Region 2	Region 3
Interval I	$\theta=0^\circ (=180^\circ)$ 	<ul style="list-style-type: none"> • compr. in fibre direction • lateral force on fibres due to γ <p>→ buckling and bending, depending on γ</p> <p>→ peeling of matrix</p>	<ul style="list-style-type: none"> • compr. in fibre direction • lateral force on fibres due to γ • peeling of matrix <p>→ interlaminar crack</p>	<ul style="list-style-type: none"> • bouncing back (low intensity) • friction between tool/CFRP
Interval II	$15^\circ < \theta < 75^\circ$ 	<ul style="list-style-type: none"> • compr. on fibres • shear in matrix <p>→ shear plane</p>	<ul style="list-style-type: none"> • initial fibre separation due to bending • shear in matrix • further bending of fibres and ploughing under cutting edge • possibly secondary breakage of fibres 	<ul style="list-style-type: none"> • bouncing back (high intensity) • Intensive friction between tool/CFRP
Interval III	$\theta=90^\circ$ 	<ul style="list-style-type: none"> • shear force on fibres and compr. perpend. to fibre axis • shear force and compr. on matrix 	<ul style="list-style-type: none"> • compr. perpendicular to fibre axis • shear force and compr. on matrix • bending of initially broken fibres and ploughing under cutting edge 	<ul style="list-style-type: none"> • bouncing back (medium intensity) • Intensive friction between tool/CFRP
Interval IV	$105^\circ + \gamma < \theta < 165^\circ$ 	<ul style="list-style-type: none"> • compr. on fibres (buckling) • bending of fibres • peeling of matrix 	<ul style="list-style-type: none"> • compression of fibres → buckling • bending of fibres • peeling of matrix → interlaminar crack 	<ul style="list-style-type: none"> • bouncing back (very low intensity)

Fig. 2.9. Schematic view of sub-models and chip formation mechanisms in each of the four fibre orientation intervals [19].

Tool flank wear is considered in their force model, and the cutting edge geometry with wear is defined by five parameters: l_α , l_γ , γ^* , α^* , b_c , shown in Fig. 2.10. These parameters describe the worn cutting edge geometry with a “straight line – ellipse – straight line” approach. The proposed model has a good agreement with experimental data for different fiber orientations and tool geometry in different tool wear state.

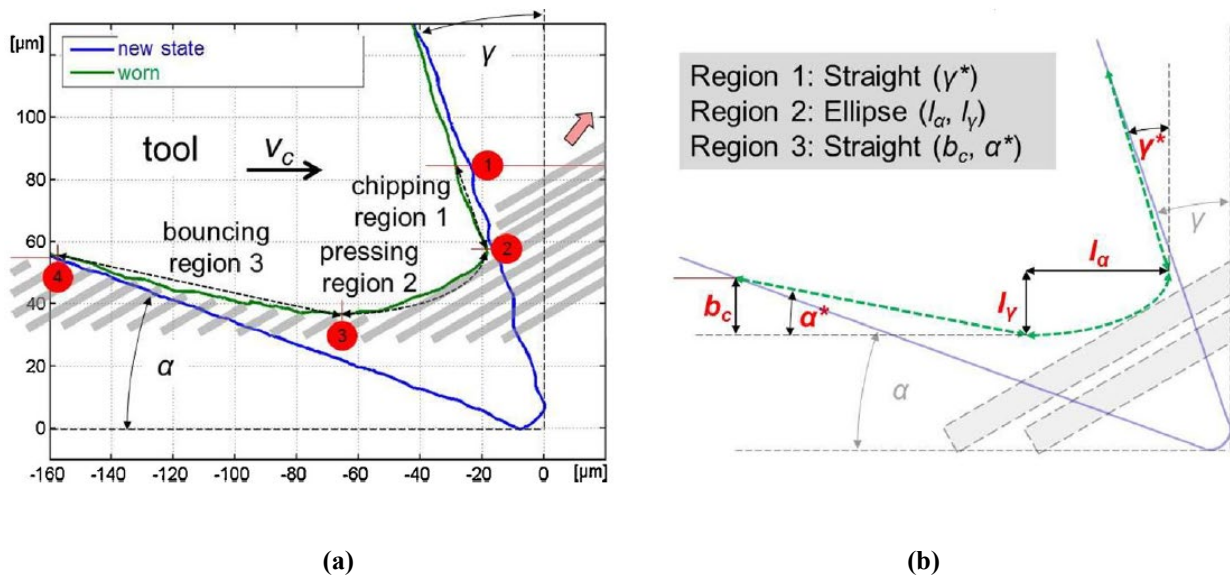


Fig. 2.10. Schematic view of (a) Exemplary new (blue) and worn (green) cutting edge profile and (b) evaluation of current micro geometry with five micro-geometry parameters [19].

The micro-scale analytical model considers the fiber, matrix and interface individually, therefore, the predicted results reveal more information on the fiber deformation compared to macro-scale model. However, the micro-scale analytical model still cannot predict the whole chip formation process, and different analytical models must be established respectively for different ranges of fiber orientation angles.

2.2 Experimental studies

As shown above, analytical models are accurate in predicting cutting forces only for a limited range of fiber orientation angles. Moreover, analytical studies cannot provide enough information about chip formation and surface morphology. With the help of high-speed camera and SEM, experimental studies allow the investigation of the chip formation, surface finish and cutting forces at the same time.

Koplev et al. [20] studied chip formation mechanisms and surface quality of machined surface by performing cutting experiments on UD-CFRP composite with $0^\circ/90^\circ$ fiber orientation angle. Based on macrochip methods, they investigated the chip dimensions, surface morphology and cutting forces with a “quick stop” device. They found that better surface finish can be obtained when the cutting direction is parallel to the fiber orientation. The chip formation is due to brittle failure of both matrix and fibers rather than plastic deformation. When the fiber orientation angle is 90° , the tool movement causes bending of the fibers, and then fracture to form the chips. In addition, the fiber-matrix debonding occurs due to the pressure on the composite below the tool. When the fiber orientation angle is 0° , because of the pressure of the cutting tool, a crack is often observed in front of the tool tip, resulting in the formation of the next chip. Fig. 2.11 shows the chip formation when the fiber orientation angles are 0° and 90° respectively.



Fig. 2.11. Cross-section of 'quick-stop' specimens showing the notch formed by the tool: (a) machined perpendicular to the fibers; (b) machined parallel to the fibers [20].

Wang, et al [21] observed three different cutting mechanisms in orthogonal cutting using high-speed camera and macro-chip technique. For 0° fiber orientation angle, chip formation is contributed by fracture along the fiber/matrix interface, and then, bending stress results in fracture perpendicular to the fiber direction. For fiber orientation angle ranging from 0° to 75° , chip formation mechanisms include compression induced shear perpendicular to the fiber axis. For fiber orientation angle larger than 90° , both in-plane and out-of-plane shear fracture occurred along the fibre/matrix interface, leading to severe macro deformation. The schematics of the chip formation mechanism are shown in Fig. 2.12.

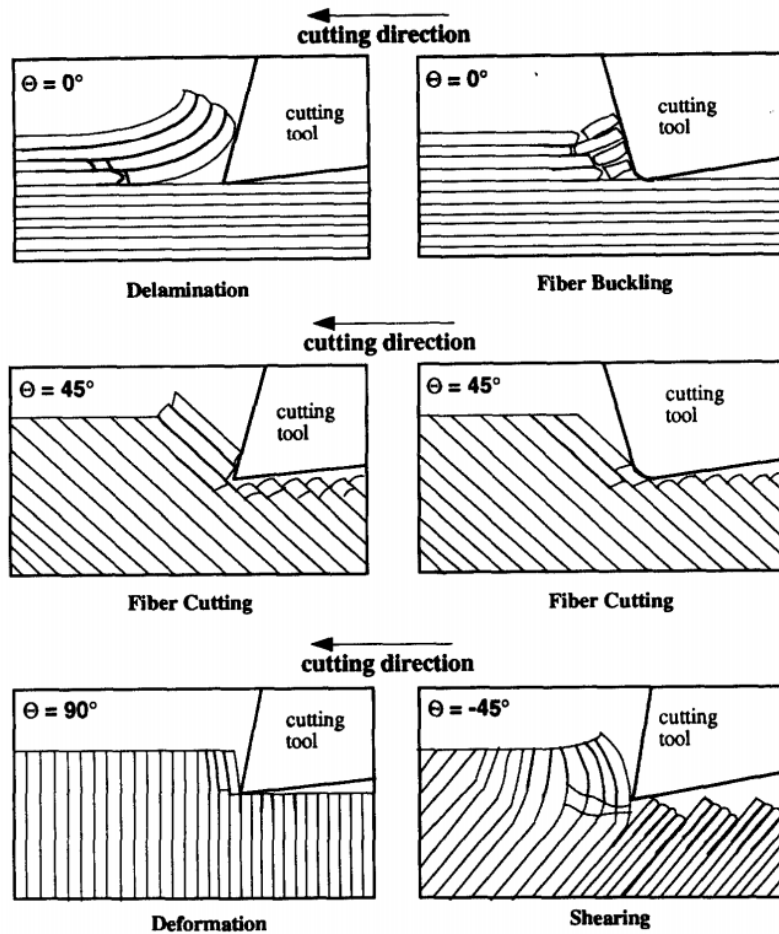


Fig. 2.12. Cutting mechanisms in the orthogonal cutting [21].

Based on the experimental investigations on orthogonal cutting of UD-FRP composite, Wang and Zhang [22] found that the surface roughness, subsurface damage and cutting forces change significantly with the fiber orientation angle. Severe subsurface damage is produced when fiber orientation angle is larger than 90° . Furthermore, significant bouncing back of materials after cutting occurs due to the bending of the fibers. The type of deformation is also influenced by uncut chip thickness. When fiber orientation angle is higher than 90° and uncut chip thickness is comparable to tool tip radius (Fig. 2.13(b)), compressive axial force is applied to the fibers; therefore, the finished surface normally has many protruded fibers, leading to a larger surface

roughness. When the uncut chip thickness is larger than tool tip radius (Fig. 2.13(c)), the cutting force perpendicular to the fiber axis pushes the fiber outwards, leading to a more severe fiber bending and fiber-matrix debonding.

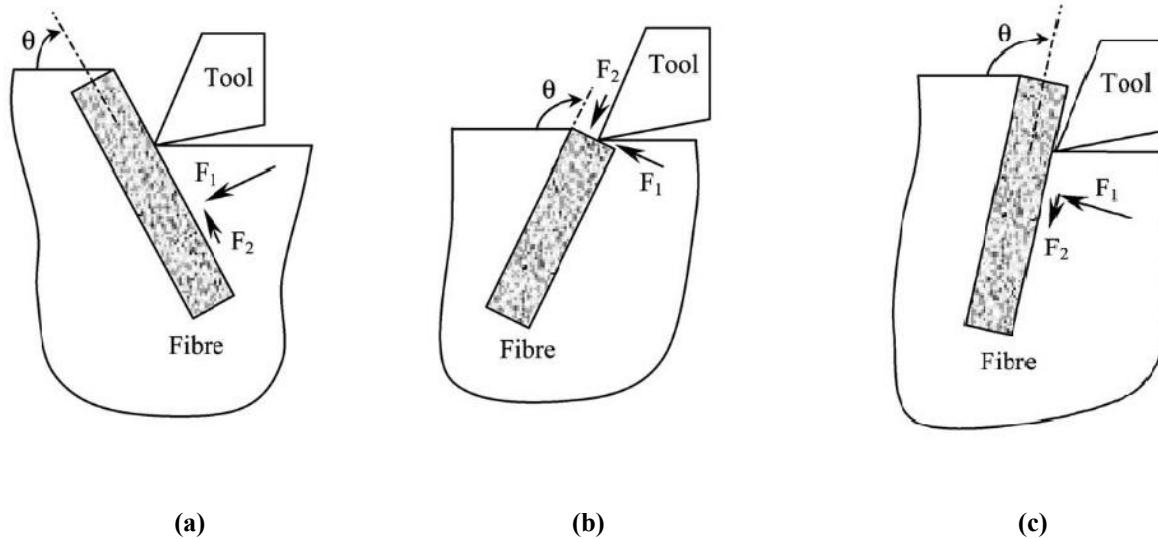


Fig. 2.13. Deformation mechanisms based on depth of cut [22].

Experimental investigation provides reliable and complete information of chip formation, cutting force generation, and surface property. However, it is an expensive and time consuming procedure. When the cutting parameters change, different experiments have to be performed to obtain the corresponding results. Moreover, in most of the cutting conditions, the chips are in the form of powder, which may cause harm the machining operator's health.

2.3 Numerical studies

With the development of finite element method (FEM) and computational capability, numerical simulation has become a promising technique to analyze the cutting mechanism for CFRP. Two

major types of FE models have been developed: micro-scale and macro-scale mechanical model, similar to the analytical mechanics modeling approach. The simulation results from micro-scale model reveal more details on the material removal mechanism compared to macro-scale model, while the computational cost of micro-scale model is much higher due to the requirement of fine mesh in the FE model.

2.3.1 Macro-mechanical numerical modeling

Arola and Ramulu [23] performed finite element simulation of orthogonal cutting of FRP composites. A 2-D EHM model (shown in Fig. 2.14) is used to analyze the orthogonal cutting process by defining two fracture mechanisms (i.e. maximum stress and Tsai-Hill criteria) for a single chip formation. The simulated tangential forces match well with the experiment results, while certain discrepancy was observed for thrust force. Comparison between the experimental cutting forces and the simulation results are shown in Fig. 2.15.

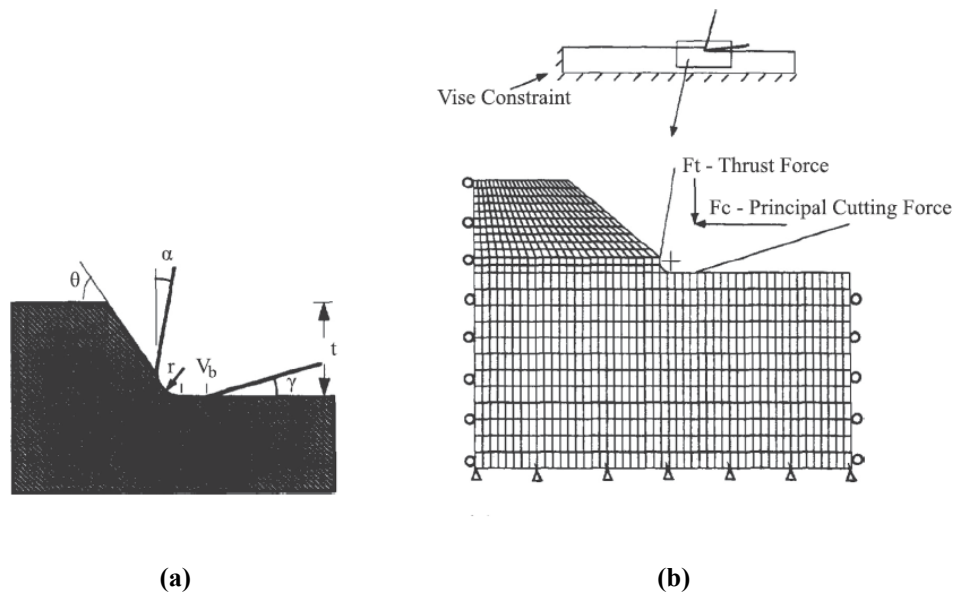


Fig. 2.14. The finite element model with (a) Tool geometry; (b) Boundary conditions and cutting forces [23].

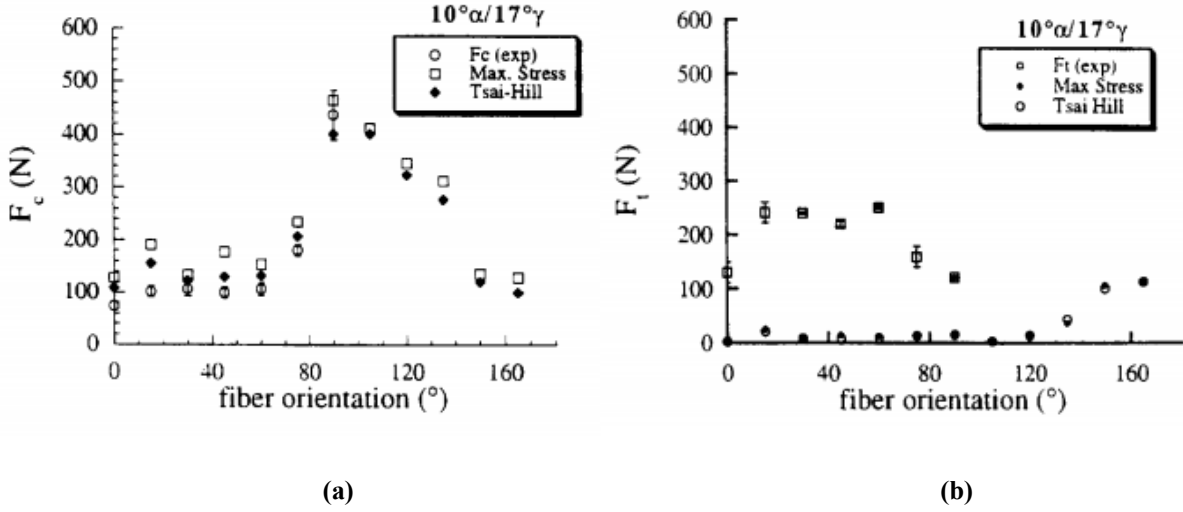


Fig. 2.15. Comparison between experimental cutting forces and simulations, 0.120 mm depth of cut, 10° rake angle, 17° clearance angle: (a) Principal cutting force; (b) Thrust force [23].

Based on quasi-static plane strain deformation conditions, Mofid and Zhang [24] developed a 2D EHM cutting model with Tsai-Hill failure criterion for simulating chip formation. The EHM properties in the model were obtained by using Chamis model [25]. The Chamis micromechanical model determines the elastic properties of EHM using elastic properties of fiber and matrix respectively as:

$$\begin{aligned}
 E_{11} &= V^f E_{11}^f + V^m E^m \\
 E_{22} &= \frac{E^m}{1 - \sqrt{V^f} (1 - E^m / E_{22}^f)} \\
 \nu_{12} &= V^f \nu_{12}^f + V^m \nu^m \\
 G_{12} &= \frac{G^m}{1 - \sqrt{V^f} (1 - G^m / G_{12}^f)} \\
 G_{23} &= \frac{G^m}{1 - \sqrt{V^f} (1 - G^m / G_{23}^f)}
 \end{aligned} \tag{2.9}$$

where V^f and V^m correspond to the volume fraction of fiber and matrix, respectively.

Mofid and Zhang [24] observed the maximum cutting forces when fiber orientation is about 100° through FE simulations. Fig. 2.16 shows the discrepancy between their simulated results and the experimental data obtained by Wang and Zhang [22]. Their model was in good agreement with experimental results, and no remarkable effect was found for the rake angle varying from 0° to 20° . It is concluded that the difference between the simulated and experimental results are caused by the EHM assumption of the composite materials.

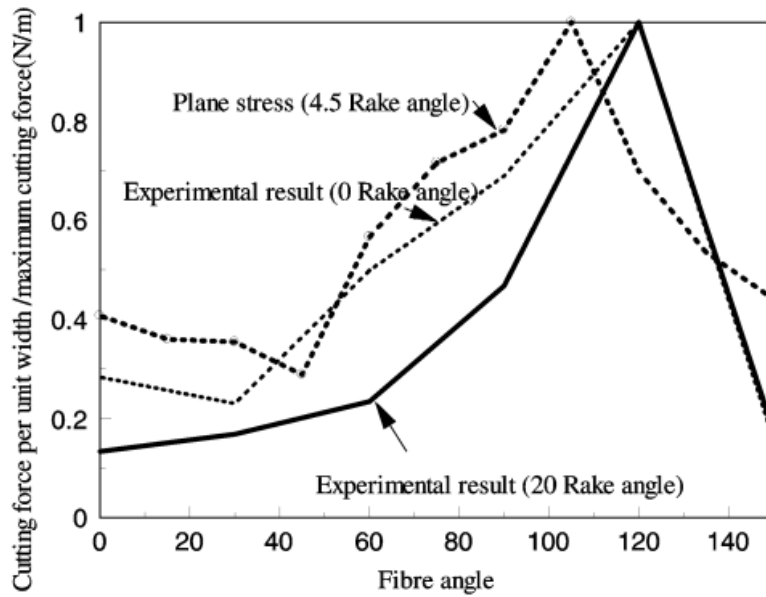


Fig. 2.16. Cutting forces versus fiber orientation for anisotropic EHM [24].

Lasri et al. [26] conducted FE simulations to compare the effects of different failure criteria (i.e. Hashin criterion, Maximum stress criterion and Hoffman criterion)) on chip formation and subsurface damage in machining of CFRP. It is shown that the chip formation always consists of different failure modes, such as fiber-matrix debonding and fiber breakage. As shown in Fig. 2.17(a), the simulated principal cutting force using Hashin criterion were closer to the experiments compared to other failure criteria; however, the simulated thrust cutting force had a big difference

with experiments no matter which failure criterion was used. Their research also showed that fiber orientation is the dominant factor that determines the extent of subsurface damage. Cutting with 30° fiber orientation results in the minimum subsurface damage.

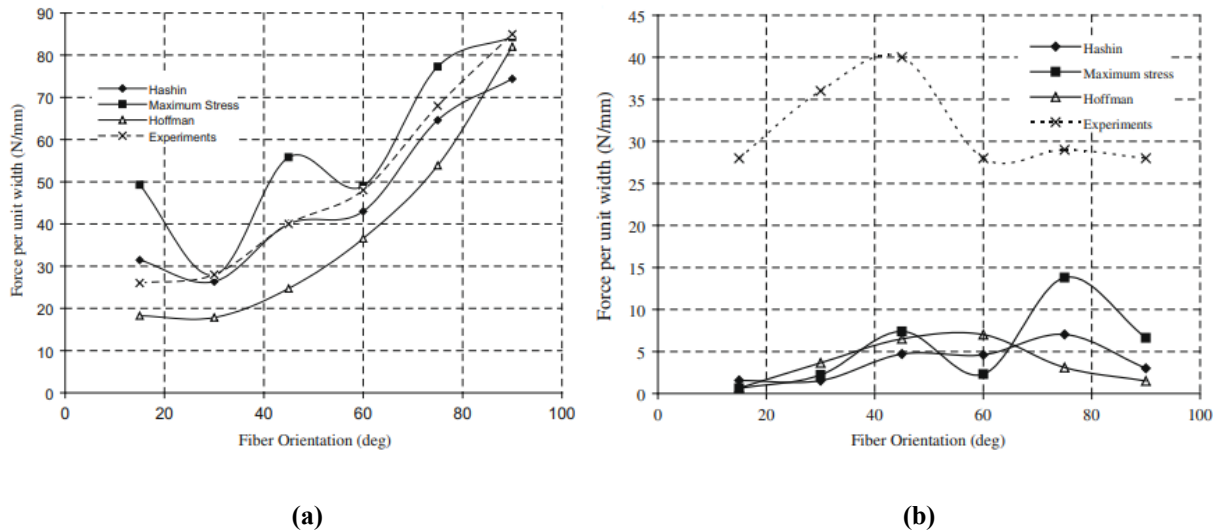


Fig. 2.17. Comparison between experimental cutting forces and simulations: (a) Principal cutting force; (b) Thrust force [26].

2.3.2 Micro-mechanical numerical modeling

In micro-mechanical numerical model, fiber, matrix and interface are modeled separately, hence it is able to simulate the deformation of individual constituent and at the interface. A FE model consisting of a single fiber and surrounding matrix was developed by Nayak et al. [27] in order to save computational cost in the simulations (shown in Fig. 2.18). Fig. 2.19 shows that the simulated principal and thrust cutting forces agree well with the experimental results. It is found that the fiber breaks in tension instead of compression in all fiber orientation angles. When tool rake angle is 30° , a minimum surface damage can be obtained. However, their model was only applicable when

fiber orientation angle is smaller than 90° fiber orientation, and the matrix damage was neglected in determining the cutting forces.

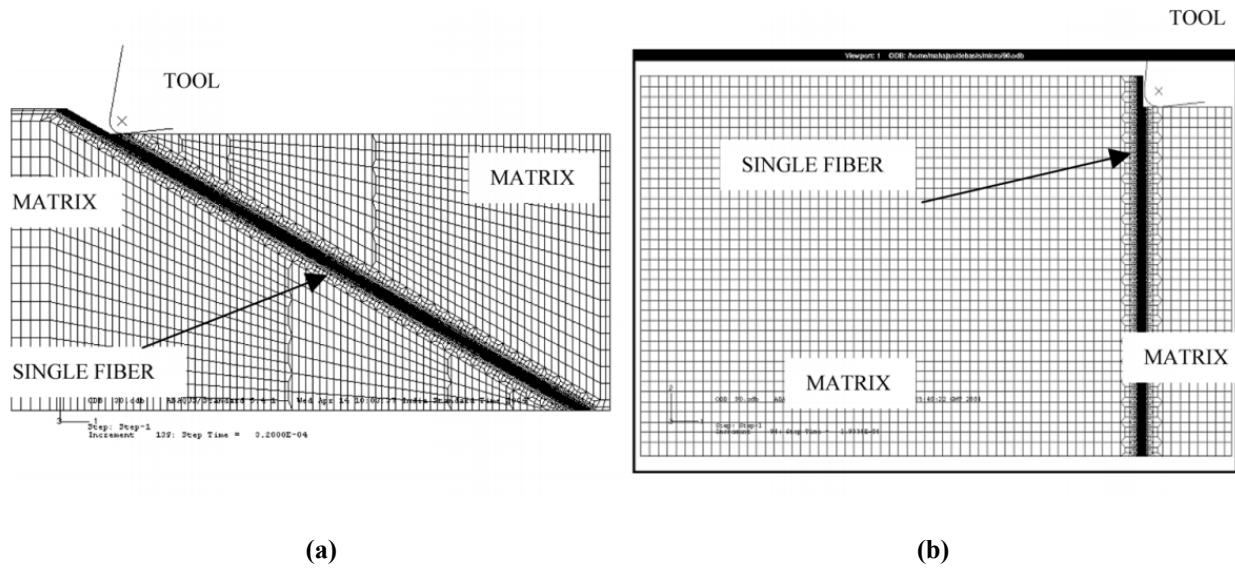


Fig. 2.18. Finite element model of a single fiber with surrounded matrix; (a) 30° fiber orientation, (b) 90° fiber orientation [27].

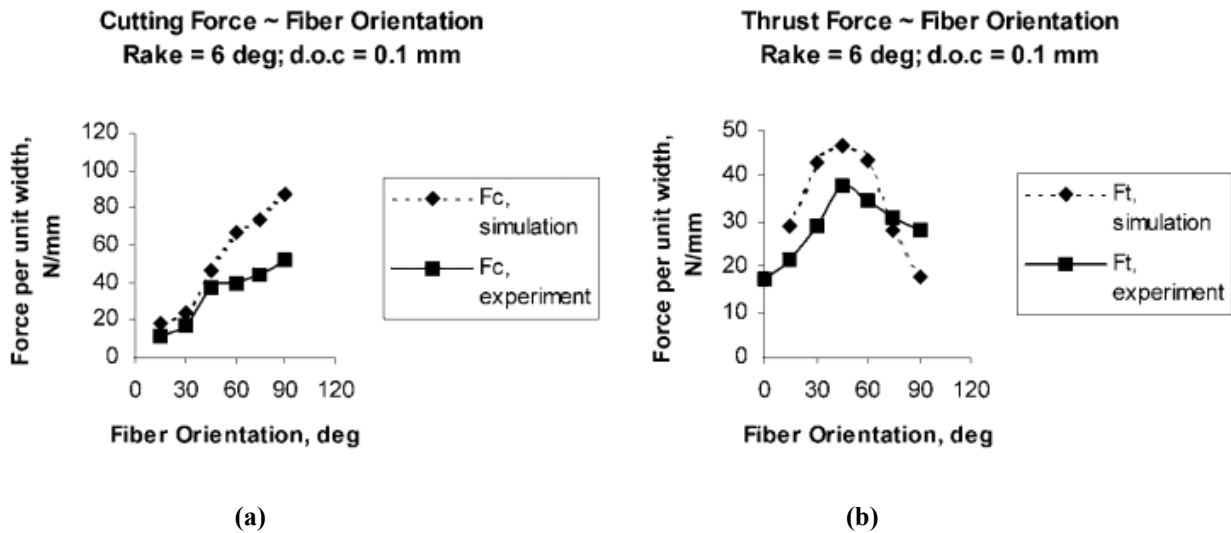


Fig. 2.19. Comparison between experimental cutting forces and simulations: (a) Principal cutting force; (b) Thrust force [27].

Rao et al. [28] combined micro-scale and macro-scale models to simulate 2-D orthogonal cutting of FRP composites and predict the cutting forces (Fig. 2.20), thus have the advantage from both models: low computational cost and capability of predicting subsurface damage and cutting forces. They assumed that the fiber is pure elastic and the matrix is elasto-plastic material. Based on the work from Nayak et al. [27], they added matrix damage criterion and fiber-matrix interface (i.e. cohesive zone model) in the model. However, their model mainly focused on simulating the workpiece material which is close to tool tip, while the whole chip formation process cannot be simulated.

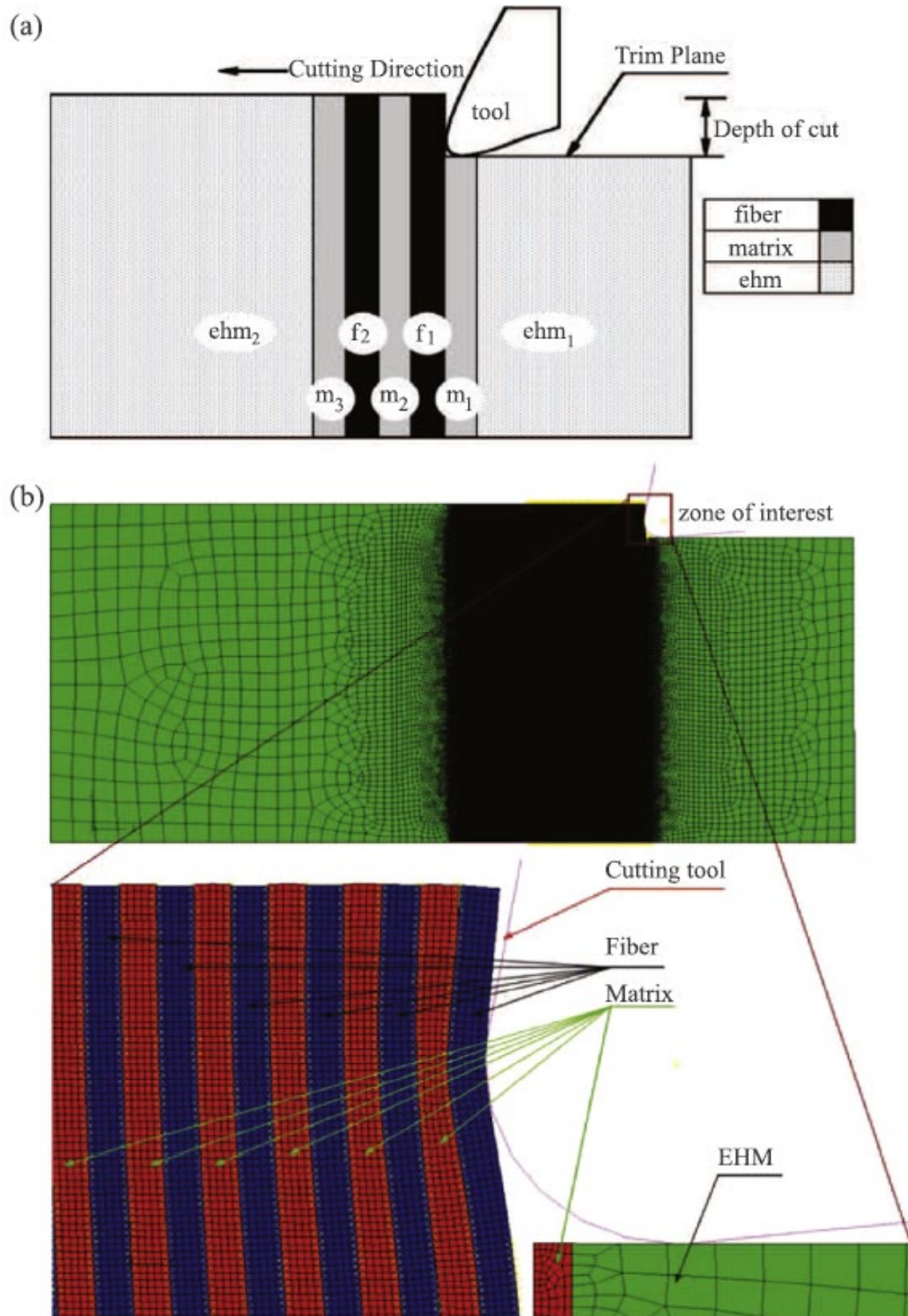


Fig. 2.20. (a) Schematic view of fiber, matrix and EHM zones used in finite element modeling; (b) 25 fiber, 26 matrix and 2 EHM layers used in finite element model [28].

Calzada et al. [29] implemented velocity-based boundary condition for tool in 2D micro-scale model, and assigned both tensile and compressive damage models to continuum cohesive elements. They used a velocity-based boundary condition instead of displacement to establish a dynamic cutting model, which is able to predict and analyze the chip formation and material failure mechanisms. The model predicted the fiber failure, characteristic chip length and forces of UD-FRP in all fiber orientation angles (see Fig. 2.21).

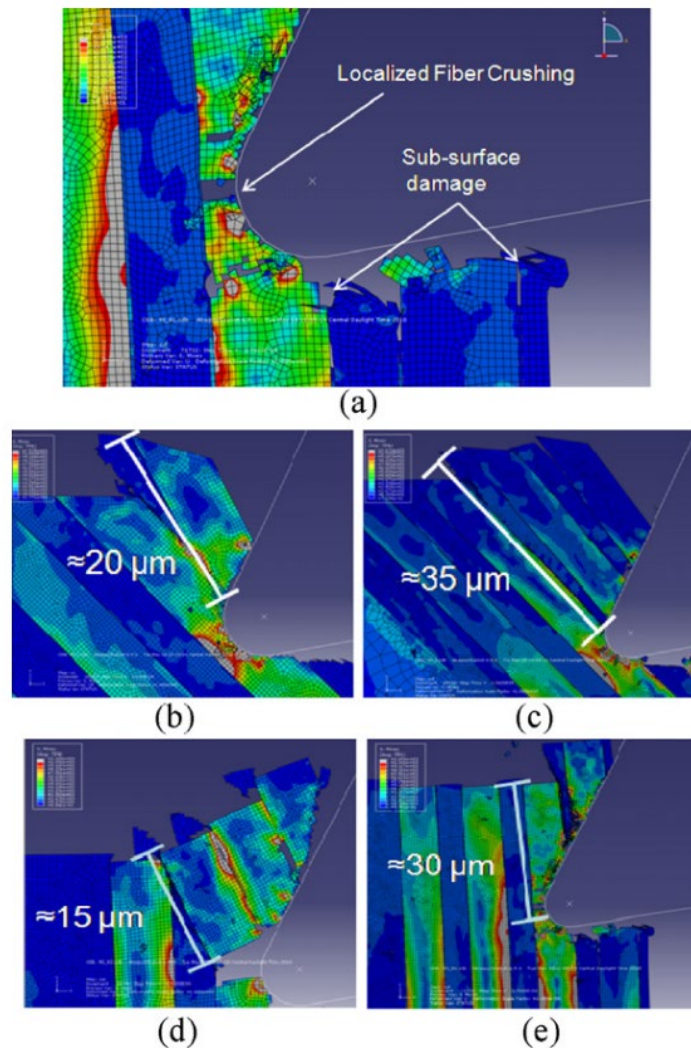


Fig. 2.21. Simulation results with (a) 45° and 90° failure nodes; (b) 45° , $15 \mu\text{m}$ depth of cut; (c) 45° , $30 \mu\text{m}$ depth of cut; (d) 90° , $15 \mu\text{m}$ depth of cut; (e) 90° , $30 \mu\text{m}$ depth of cut [29].

Using a 3-D micro-scale FE model, Xu et al. [30,31] investigated the effect of elliptic vibration-assisted (EVA) cutting on material removal mechanism and subsurface damage in orthogonal cutting of FRP composites. The elliptic tool tip motion and proposed 3D microstructure-based FE model with EVA cutting are shown in Fig. 2.22. They found that the cutting force and subsurface damage reduced with added vibration significantly. Moreover, EVA cutting is also able to extend the cutting tool life by reducing the crater and flank wear rates.

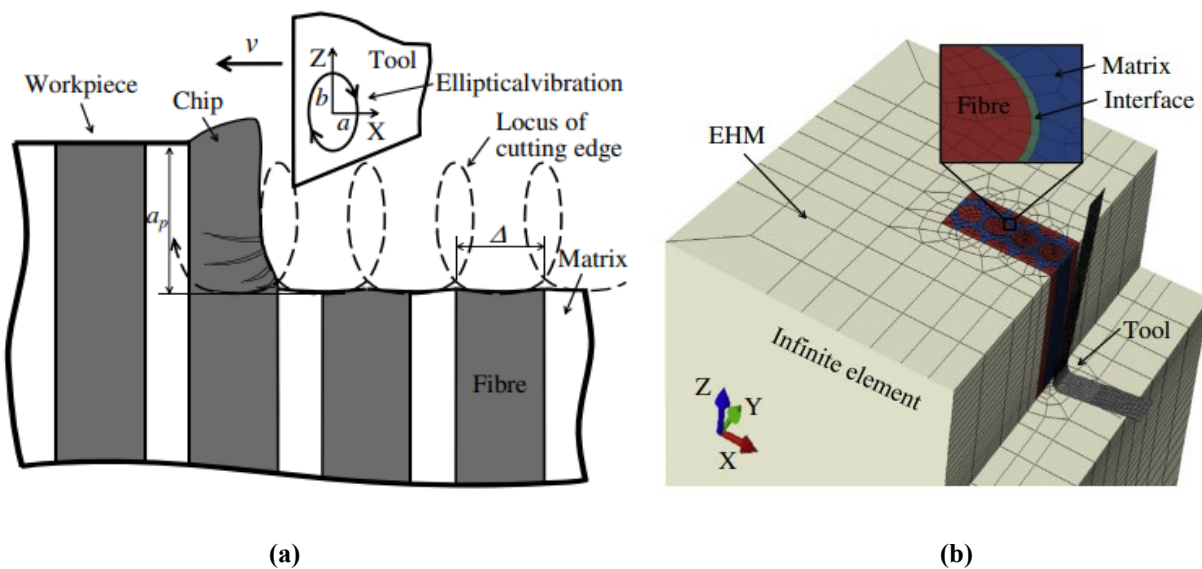
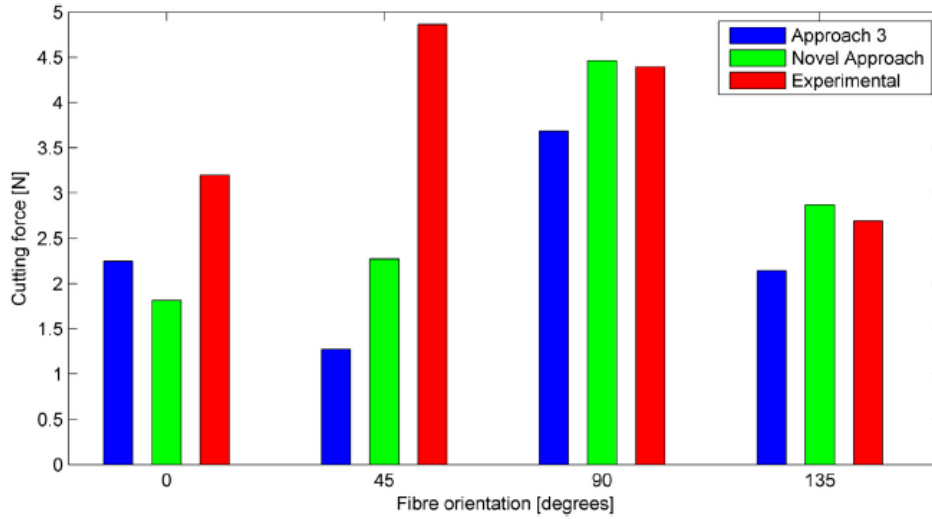


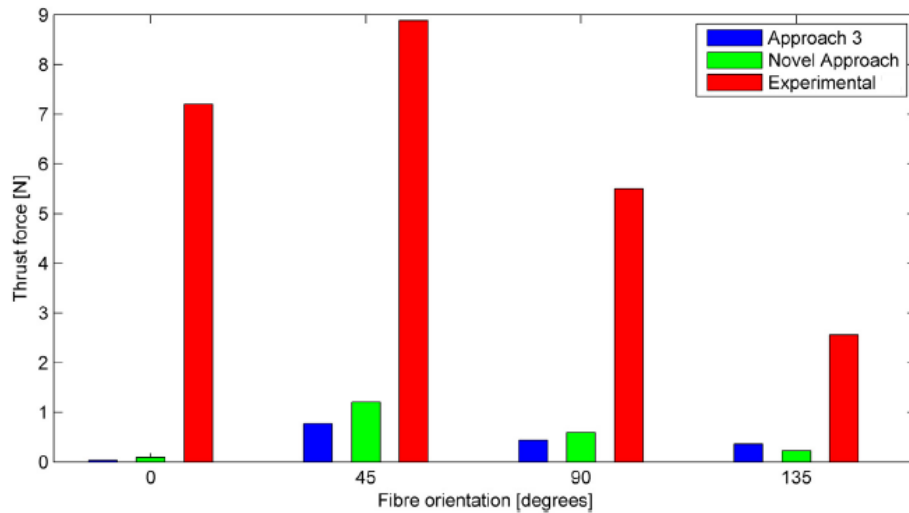
Fig. 2.22. Illustration of (a) EVA cutting of FRP composite and (b) its FE micro-scale model [30].

Abena et al. [32] developed a 3-D micro-scale model of orthogonal cutting on CFRP based on traction-separation law for the cohesive zone. Different interface modeling methods, i.e. (zero thickness cohesive elements approach, small thickness cohesive elements approach, and surface based cohesive behaviour approach, were compared in the simulations for cutting force prediction. It is shown that the simulations based on zero thickness cohesive elements approach provide better agreement with experimental results in cutting forces prediction compared to the other two

approaches, as shown in Fig. 2.23(a). However, the simulated thrust forces are still inaccurate when compared with experiments (shown in Fig. 2.23(b)).



(a)



(b)

Fig. 2.23. (a) Cutting Force and (b) thrust force comparison for Novel Approach and Approach 3 against experimental results [32].

2.4 Oblique cutting theory for metal alloys

Since there is no oblique cutting theory existing for machining CFRP. This section only presents oblique cutting model for metal alloys. Based on the classic oblique model proposed by Armarego and Whitfield [33], the resultant cutting forces F_c in three directions are expressed as [7]:

$$\begin{aligned}
 F_{tc} &= bh \cdot \left[\frac{\tau_s \frac{\cos(\beta_n - \alpha_n) + \tan i \tan \eta \sin \beta_n}{\sin \phi_n}}{\sqrt{\cos^2(\phi_n + \beta_n - \alpha_n) + \tan^2 \eta \sin^2 \beta_n}} \right] \\
 F_{fc} &= bh \cdot \left[\frac{\tau_s \frac{\sin(\beta_n - \alpha_n)}{\sin \phi_n \cos i}}{\sqrt{\cos^2(\phi_n + \beta_n - \alpha_n) + \tan^2 \eta \sin^2 \beta_n}} \right] \\
 F_{rc} &= bh \cdot \left[\frac{\tau_s \frac{\cos(\beta_n - \alpha_n) \tan i - \tan \eta \sin \beta_n}{\sin \phi_n}}{\sqrt{\cos^2(\phi_n + \beta_n - \alpha_n) + \tan^2 \eta \sin^2 \beta_n}} \right]
 \end{aligned} \tag{2.10}$$

where τ_s is shear yield stress, ϕ_n is the normal shear angle, α_n is the normal rake angle, i is the oblique angle, η is the chip-flow angle. F_{tc} , F_{fc} and F_{rc} are the resultant cutting forces in cutting, thrust and normal direction, respectively. β_n is expressed by:

$$\tan \beta_n = \tan \beta_a \cos \eta \tag{2.11}$$

where β_a is the average friction angle in oblique cutting.

In order to obtain resultant cutting forces, the normal shear angle ϕ_n and the normal rake angle α_n in oblique cutting are assumed to be equal to the shear angle and rake angle in orthogonal cutting. The shear yield stress τ_s and the average friction angle β_a are assumed to be the same in orthogonal cutting and oblique cutting [7]. Also, based on the Stabler's rule [6], the chip-flow angle η is assumed to be equal to the tool inclination angle i . Therefore, the resultant forces from oblique cutting can be obtained by evaluating the shear angle, average friction angle and shear yield stress in orthogonal cutting process.

However, the Stabler's theory in metal cutting is inapplicable to CFRP cutting. The chips in machining CFRP are mostly in the form of powders, and the chip morphology highly depends on the fiber orientation angle. These factors are not considered from Stabler's theory. Although orthogonal-to-oblique cutting theory for metal cutting has been used for decades and verified by extensive experimental studies, oblique cutting of CFRP still requires further investigation, which is the focus of this thesis.

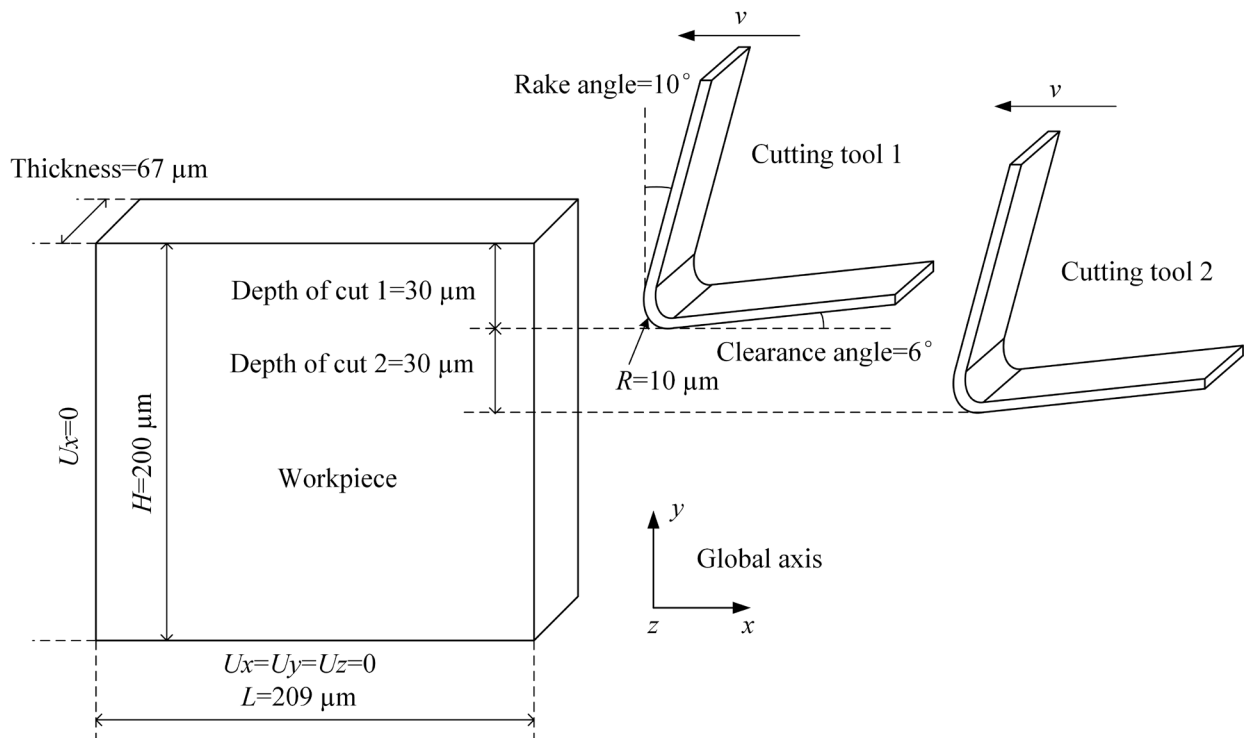
Chapter 3: Finite Element Modeling

3.1 Geometry and Process Parameters in the FE model

The oblique angle causes the fiber and matrix deformations to occur in an out-of-plane direction, and cutting forces are generated in all three directions. Therefore, a 3-D micro-scale FE model consisting of fiber, matrix, and interface individually is developed. The FE model is based on the software ABAQUS/Explicit. Fig. 3.1 shows the schematic of the FE model and the associated boundary conditions. The cutting tool is modeled as a rigid body, because the elastic modulus of the cutting tool material (tungsten carbide) is three times higher than the elastic modulus of carbon fiber. The tool edge radius (r) is 10 μm , the tool rake angle (α) is 6° , and the clearance angle (γ) is 5° . A reference point is defined on the cutting tool to control the cutting motion with provided cutting speed. In order to simulate sequential cutting, two cutting tools are placed near the workpiece with a certain distance, as shown in Fig. 3.1(a). They move with a constant speed in the cutting direction simultaneously. Therefore, after the first tool finishes the cutting, the second tool conducts cutting on the CFRP material which includes damage and residual stress caused by the previous cutting. The vertical distance of the two cutting tools is 30 μm , which is a typical value of feedrate in milling of CFRP.

Unidirectional CFRP materials are defined in the micro-scale FE model. The dimensions of the UD-CFRP workpiece are 209 μm \times 67 μm \times 200 μm (length \times width \times height). The whole CFRP workpiece consists of 25 fibers in the cutting velocity direction, and 8 fibers in the transverse direction, thus 200 fibers in total. The distance between neighboring fiber layers is 1.35 μm , fulfilling the specification of the CFRP material with a 55% fiber volume fraction. The

displacement at the bottom of the workpiece is constrained in all directions. The fiber orientation angle (θ) is defined as the angle between fiber and tool velocity direction. The diameter (D) of the fiber is $7\ \mu\text{m}$. The workpiece is meshed by C3D8R and C3D6 elements with average element size of $1.5\ \mu\text{m}$, and the cutting tools are meshed by C3D8R elements with a coarser size of $6\ \mu\text{m}$. In order to reduce the computational cost, mass scaling is used in this study. It should be noted that although heat generation is expected to influence the matrix property in the cutting process, this thesis is focused on the effect of oblique angle and sequential cutting rather than temperature, therefore, low cutting speed ($v = 0.5\ \text{m/min}$) is defined in the model to neglect the heat effect occurring at higher cutting speed. The geometry of the cutting tool and the workpiece, and the cutting process parameters are summarized in Table 1.



(a)

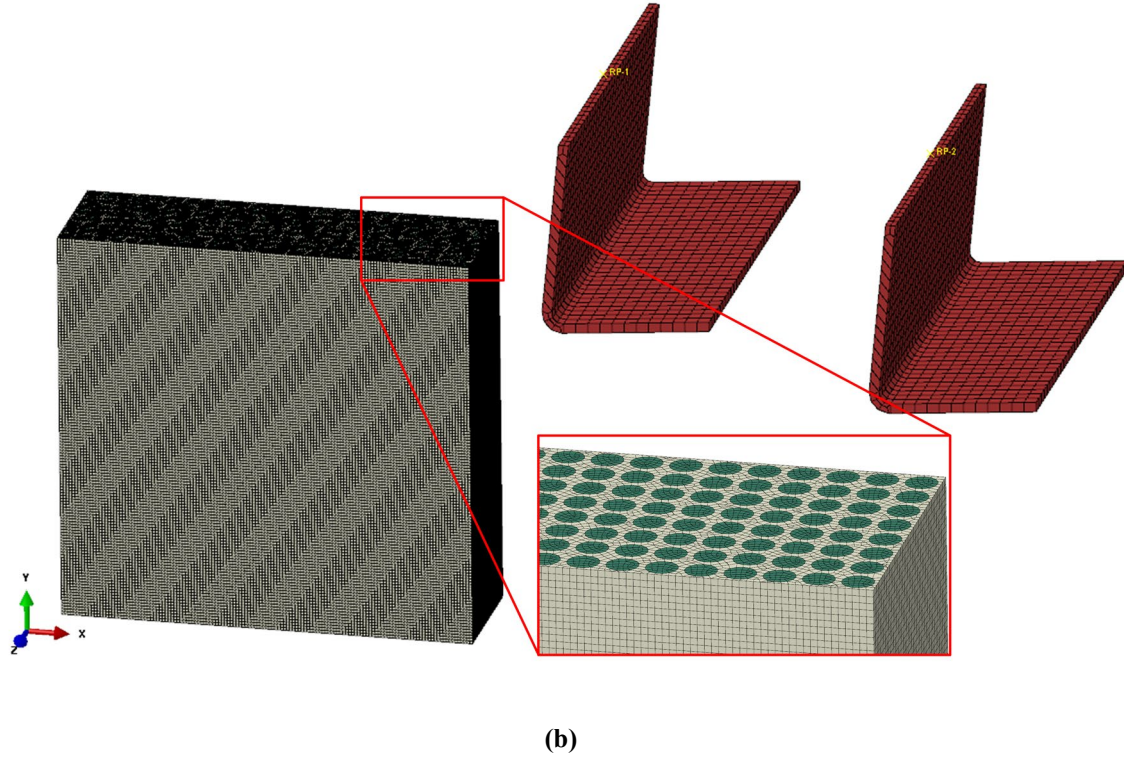


Fig. 3.1. (a) Schematic illustration of sequential cutting on a UD-CFRP composite, (b) the microstructure-based FE model for cutting UD-CFRP.

Table 1 Parameters used in the FE model and simulations.

	Parameter	Values
UD-CFRP composites	Workpiece dimensions	209 μm \times 200 μm \times 67 μm
	Rake angle (α)	6 $^\circ$
Tool geometry	Clearance angle (γ)	5 $^\circ$
	Edge radius (r)	10 μm
Process parameters	Uncut chip thickness (h)	30 μm
	Fiber orientation (θ)	0 $^\circ$, 45 $^\circ$, 90 $^\circ$
	Cutting speed (v)	0.5 m/min

3.2 Material definition in the FE model

The material definition in the FE model includes the failure models of carbon fiber, epoxy matrix, and the failure criterion at the fiber/matrix interface. With defined material properties, the FE model is able to predict chip formation, surface generation, and cutting forces in the oblique and sequential cutting process. Material properties are based on UD-CFRP sheet (UTS 700 carbon fiber impregnated with NCT 304-1 resin matrix), which is used in the simulations and experiments in this thesis.

3.2.1 Carbon Fiber

Carbon fibers are modeled as transversely isotropic materials, and are assumed to be pure elastic without plastic deformation based on experimental investigations [26, 34, 35]. Abena et al. [32] and Yan et al. [2] also used the same type of material definition for carbon fibers in micro-scale UD-CFRP cutting simulations. In this study, the maximum stress failure criterion is used for carbon fiber. The fiber fails when the principal tensile/compressive stress exceeds the corresponding strength, expressed as [36]:

$$\left\{ \begin{array}{ll} \text{Tensile failure in longitudinal direction} & (\sigma_{11} \geq 0) \quad \left(\frac{\sigma_{11}}{X_T} \right)^2 \geq 1 \\ \text{Compressive failure in longitudinal direction} & (\sigma_{11} < 0) \quad \left(\frac{\sigma_{11}}{X_C} \right)^2 \geq 1 \\ \text{Tensile failure in transverse direction} & (\sigma_{22} \geq 0 \text{ or } \sigma_{33} \geq 0) \quad \left(\frac{\sigma_{22}}{Y_T} \right)^2 \geq 1, \left(\frac{\sigma_{33}}{Y_T} \right)^2 \geq 1, \\ \text{Compressive failure in transverse direction} & (\sigma_{22} < 0 \text{ or } \sigma_{33} < 0) \quad \left(\frac{\sigma_{22}}{Y_C} \right)^2 \geq 1, \left(\frac{\sigma_{33}}{Y_C} \right)^2 \geq 1, \end{array} \right. \quad (3.1)$$

where X_T and X_C are the tensile and compressive strength in longitudinal direction; Y_T and Y_C are the tensile and compressive strength in transverse direction. σ_{ii} is the stress tensor component of the fiber. The strength-related constants are listed in Table 2. A VUMAT user subroutine is developed and implemented into the FE model to achieve the failure criterion for carbon fiber.

3.2.2 Matrix

The matrix material of the CFRP composite in this study is epoxy resin. In the FE model, the epoxy resin is modeled as isotropic and elasto-plastic material. The elastic modulus and Poisson's ratio of the matrix material are listed in Table 2. For plastic property, Von Mises yield criterion is used, and the plastic behavior of the matrix is defined by a static stress-strain relation at room temperature [37]. The ductile damage algorithm built-in to ABAQUS is used to simulate progressive damage of the matrix material. The damage initiation criterion is defined by equivalent fracture strain. The damage progress is based on linear damage evolution law until the elements are deleted. The strength equation of matrix is shown as:

$$\sigma = \begin{cases} E\varepsilon \\ (1-D)\bar{\sigma} \end{cases} \quad (3.2)$$

where E is elasticity modulus, and $\bar{\sigma}$ represents the stress value corresponding to undamaged status. Stiffness degradation factor D is zero at damage initiation point, and it reaches unity corresponding to complete failure of the matrix element.

3.2.3 Fiber-matrix interface

In previous literature, three approaches are generally used in defining the fiber-matrix interface property: the small thickness cohesive elements approach based on traction-separation law [38], the zero thickness cohesive elements approach based on traction-separation law [39], and the surface-based cohesive behavior approach [40]. The surface-based approach implements the cohesive behavior as a contact property to avoid excessive deformation of the cohesive elements and additional computational cost. Therefore, it is typically easier to define and allows simulation for a wider range of cohesive interactions [41]. In this study, the surface-based cohesive behavior approach is applied in the FE model. Fig. 3.2 shows the linear elastic - separation behavior at the fiber-matrix interface. The undamaged response is assumed to be linear elastic followed by the initiation and evolution of damage. Uncoupled mode is used to simplify the elastic behavior, which indicates that pure normal separation does not affect cohesive stress in the shear directions, and pure shear stress with zero normal separation does not affect normal stress [32]. The elastic constitutive matrix is expressed below:

$$\mathbf{t} = \begin{Bmatrix} t_n \\ t_s \\ t_t \end{Bmatrix} = \begin{bmatrix} K_{nn} & 0 & 0 \\ 0 & K_{ss} & 0 \\ 0 & 0 & K_{tt} \end{bmatrix} \begin{Bmatrix} \delta_n \\ \delta_s \\ \delta_t \end{Bmatrix} = \mathbf{K}\delta \quad (3.3)$$

where the nominal traction stress vector \mathbf{t} consists of three components t_n , t_s and t_t , which represent the normal stress and the two shear stresses at the interface respectively. The corresponding separations are denoted by δ_n , δ_s , and δ_t .

Maximum stress criterion [36] is applied to simulate the damage at the interface. Damage is assumed to initiate when the maximum contact stress ratio reaches unity, expressed as:

$$\max \left\{ \frac{\langle t_n \rangle}{t_n^0}, \frac{t_s}{t_s^0}, \frac{t_t}{t_t^0} \right\} = 1 \quad (3.4)$$

where t_n^0 , t_s^0 and t_t^0 are the strength in normal and two shear direction respectively. When the damage initiates, the linear damage model is used to simulate the damage evolution of the cohesive interaction, expressed below:

$$D = \frac{\delta_m^f (\delta_m^{\max} - \delta_m^0)}{\delta_m^{\max} (\delta_m^f - \delta_m^0)} \quad (3.5)$$

where δ_m^{\max} refers to the maximum value of the effective separation displacement attained during the loading history, δ_m^f is the effective separation displacement at complete failure relative to the effective separation displacement δ_m^0 at damage initiation, as shown in Fig. 3.2. The parameters of the interface property are also listed in Table 2.

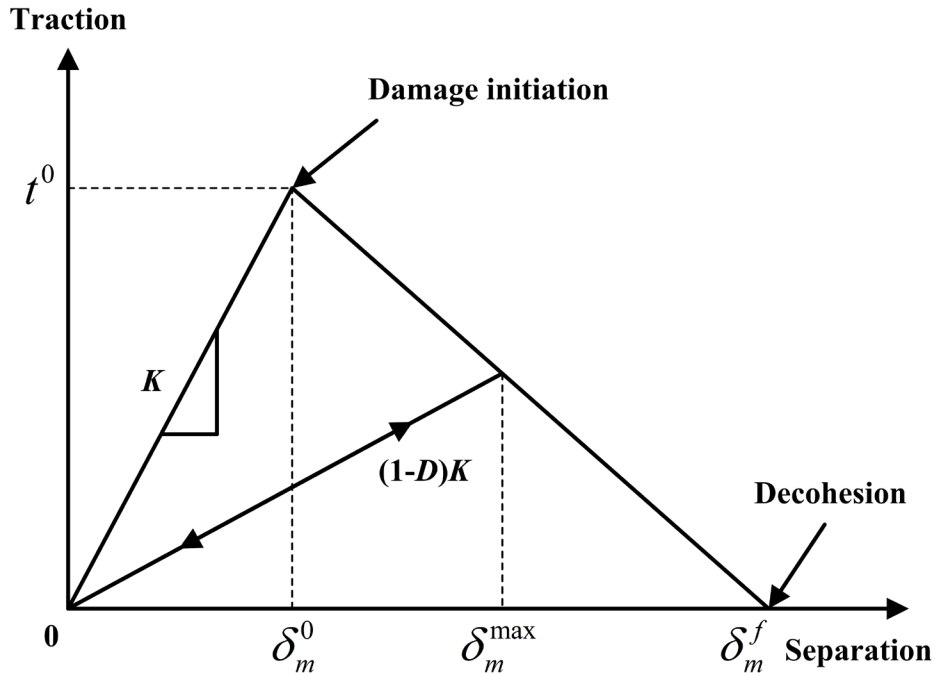


Fig. 3.2. The traction-separation response of interface under normal loading.

The penalty contact enforcement algorithm is used to model the interaction between the workpiece and the two cutting tools. The interaction property is defined as Coulomb friction with coefficient of 0.3 for all fiber orientations.

Table 2 Mechanical properties of the UD- CFRP workpiece defined in FE model.

Material	Property	Values
Fiber	Elastic Constant	$E_1 = 235 \text{ GPa}$ [32], $E_2 = E_3 = 14 \text{ GPa}$ [32], $\nu_{12} = \nu_{13} = 0.2$ [32], $\nu_{23} = 0.25$ [32], $G_{12} = G_{13} = 28 \text{ GPa}$ [32], $G_{23} = 5.5 \text{ GPa}$ [32]
	Tensile Strength	$X_t = 4.9 \text{ GPa}$ (calibrated) [2], $Y_t = 1.5 \text{ GPa}$ [2]
	Compressive Strength	$X_c = 3.96 \text{ GPa}$ [2], $Y_c = 3.34 \text{ GPa}$ [2]
Matrix	Elastic Constant	$E = 2.96 \text{ GPa}$ [32], $\nu = 0.4$ [32]
	Yield Strength	$\sigma_y = 74.7 \text{ MPa}$ [32]
Interface	Normal Strength	$\sigma_{\max} = 167.5 \text{ MPa}$ [32]
	Shear Strength	$\tau_{\max} = 25 \text{ MPa}$ [32]
	Elastic Stiffness	$K_{nn} = K_{ss} = K_{tt} = 100,000 \text{ N/mm}^3$ [2][42]
	Fracture Energy	$G_C = 0.05 \text{ N/mm}$ [32]

Chapter 4: Simulations and Experimental Verification

4.1 Experimental setup

To evaluate the developed 3-D finite element model, oblique cutting experiments on unidirectional CFRP were performed at various fiber orientation and oblique angles. Unidirectional prepreg carbon fiber sheet (UTS 700 carbon fiber impregnated with NCT 304-1 resin matrix) with fiber volume fraction of 55% and size of 15.2 mm×15.2 mm×4.8 mm was used in the experiment. Fig. 4.1 shows the experimental setup.

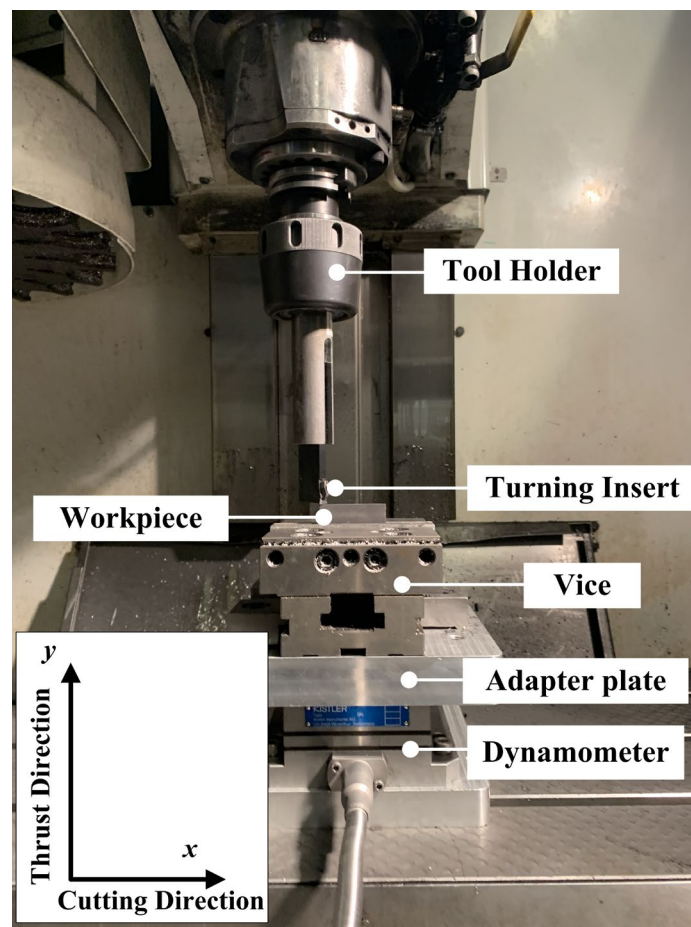


Fig. 4.1. Experimental setup for oblique cutting of UD-CFRP.

The cutting experiments were conducted on a vertical 3-axis CNC machining center (Model: FADAL 2216). Carbide turning inserts (ISO Code: TPUN 11 03 04 H13A) was fixed on the tool holder (ISO Code:177.9-2009-11), which was clamped by the spindle.

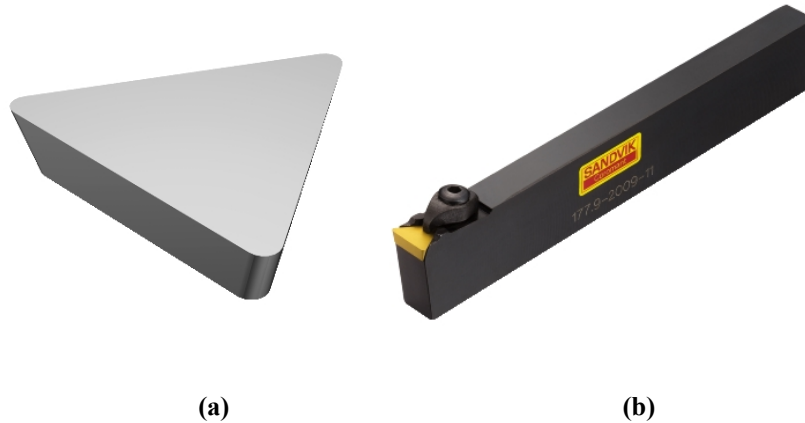


Fig. 4.2. (a) Carbide turning inserts and (b) Tool holder.

The rotational angle of the spindle shaft was adjusted according to the defined oblique angle, and then the spindle rotational motion was locked from the CNC. The length of the turning insert edge was larger than the thickness of the workpiece, so the width of cut in all the cutting tests was kept constant (0.48 mm). The CFRP workpiece and the fixture were clamped on a 3-component dynamometer (Kistler 9257B) for force measurement (shown in Fig. 4.3). A charge amplifier and data acquisition box were used to collect the force signal, and the data was recorded using CutPro software at a sampling frequency of 51,200 Hz. The cutting parameters of the experiment are the same as those used in the FE simulations provided in Table 1. In order to keep a constant uncut chip thickness value, a pre-cut was performed on the top surface of the CFRP component before each test. Therefore, all the tests in the experiments correspond to the sequential cutting configuration in the FE simulations. The tool edge was examined regularly to ensure no obvious

tool wear occurred in the experiments. After each cut, the machined chips were collected, and the chip morphology was examined using an optical microscope.

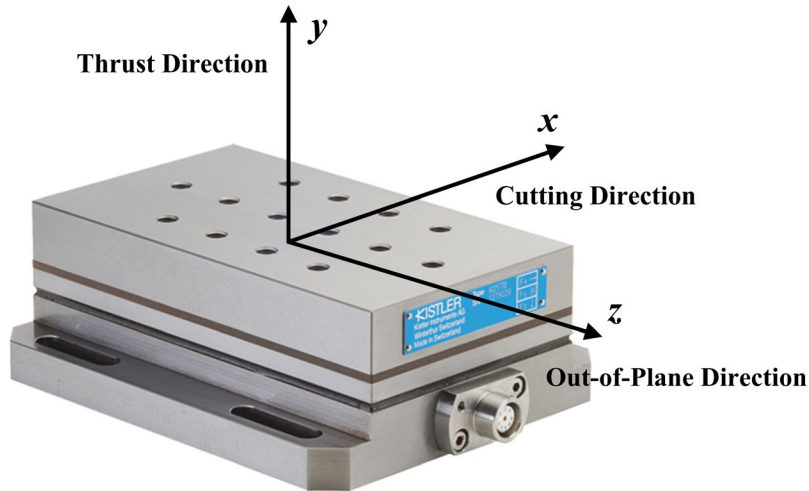


Fig. 4.3. Kistler 9257B dynamometer to capture cutting forces.

4.2 Simulations and experimental comparison

In this section, the simulated results from the FE model including chip formation and cutting forces are presented and compared to experimental results. The oblique angles (i) of 0° (orthogonal cutting), 15° , 30° , 45° , and 60° are tested. Based on Voss et al. [19] on orthogonal cutting of CFRP, the fiber orientation angles (θ) are divided into four groups according to different chip formation mechanisms: $\theta = 0^\circ$, $15^\circ < \theta < 75^\circ$, $\theta = 90^\circ$, $105^\circ < \theta < 165^\circ$. In this study, three fiber orientation angles ($\theta = 0^\circ$, $\theta = 45^\circ$, $\theta = 90^\circ$) which represent the first three groups are investigated. Cutting with 135° fiber orientation angle is not studied, since it generates severe bulk damages on the CFRP part (shown in Fig. 4.4), and is not recommended in practical machining process [34].

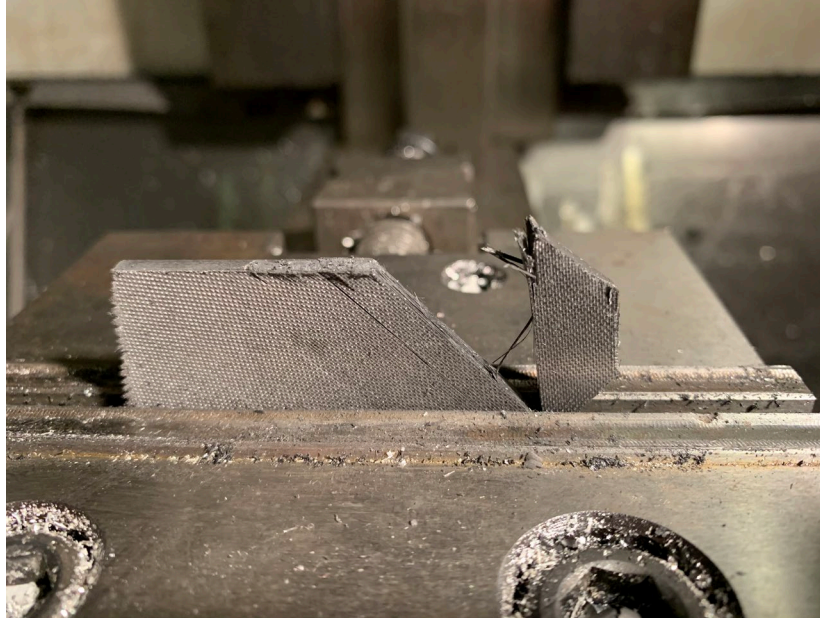


Fig. 4.4. Severe bulk damage on the CFRP part when cutting with 135° fiber orientation angle.

4.2.1 Chip formation

The mechanism of chip formation in cutting process changes for different fiber orientation angles (θ) and tool oblique angles (i). Fig. 4.5 (a) and (b) show the simulated chip formation at $\theta = 0^\circ$, with $i = 0^\circ$ (orthogonal cutting) and $i = 60^\circ$ (oblique cutting) respectively. In orthogonal cutting condition ($i = 0^\circ$), because of the high stiffness of the fibers, the contact area between the tool and the workpiece is small. Therefore, the cutting motion leads to fiber buckling, followed by a crushing failure with powder-like chips with a length typically smaller than 10 μm . At this fiber orientation angle, fiber - matrix debonding or fiber breakage below the machined surface is not obvious. However, when the tool inclination angle changes to $i = 60^\circ$ as shown in Fig. 4.5(b), most of the fibers are peeled up from the surface and slide along the tool rake face in the out-of-plane direction due to fiber bending rather than buckling, with much longer fiber chips (longer than 100

μm). The length of the chips with $i=60^\circ$ highly depends on the workpiece dimension in FE simulations. The collected chips from experiments for each case (shown in Fig. 4.6) confirm the predicted results by the FE simulations. The experimental figures show that the average length of chips in orthogonal cutting is around $8\ \mu\text{m}$, with the minimum length smaller than $1\ \mu\text{m}$ and the maximum length around $15\ \mu\text{m}$. More than 60% of the chips have the length ranging from 5 to $10\ \mu\text{m}$. When oblique angle is 60° , the length of collected chips are in millimeter scale, depending on the cutting length. The chip length results from experiments for each case (shown in Fig. 4.6) confirm the trend of chip length variation with respect to oblique angle predicted by the FE simulations.

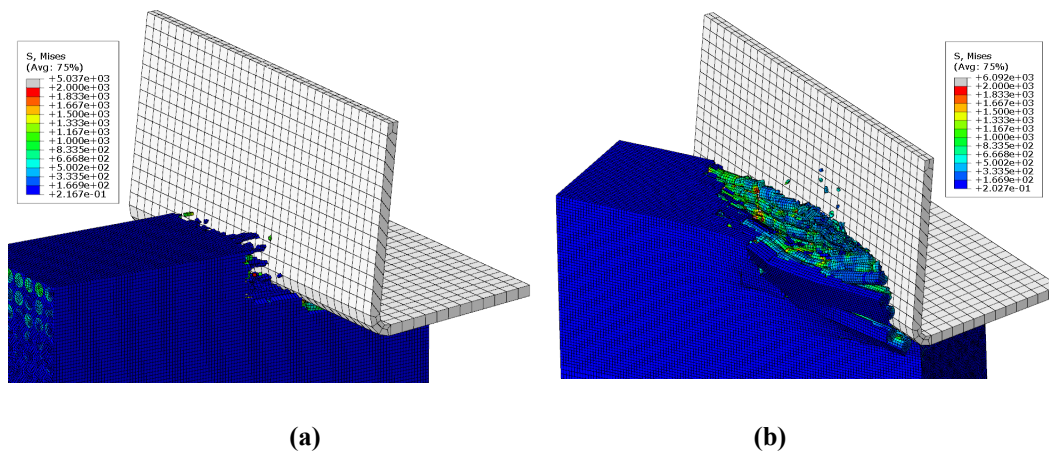
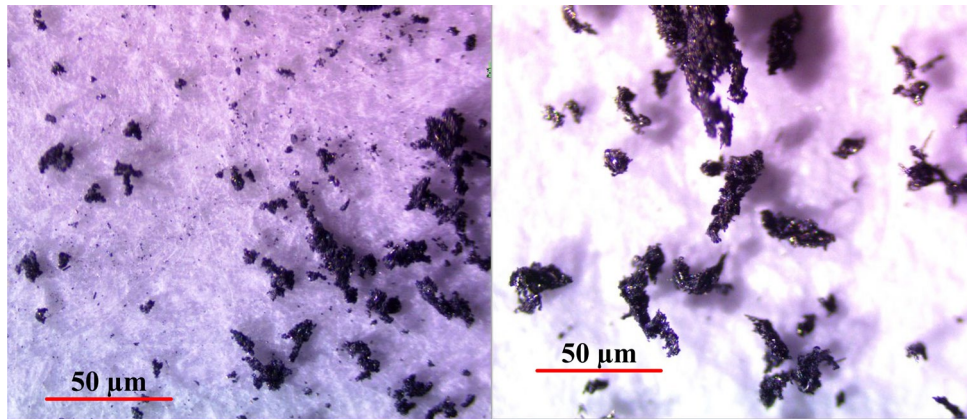
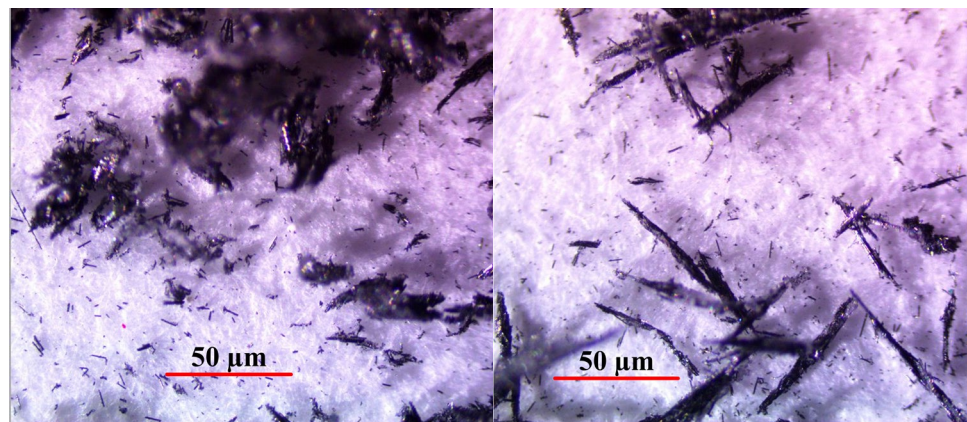


Fig. 4.5. Simulated chip formation in steady state cutting for: (a) $\theta=0^\circ$, $i=0^\circ$, (b) $\theta=0^\circ$, $i=60^\circ$.



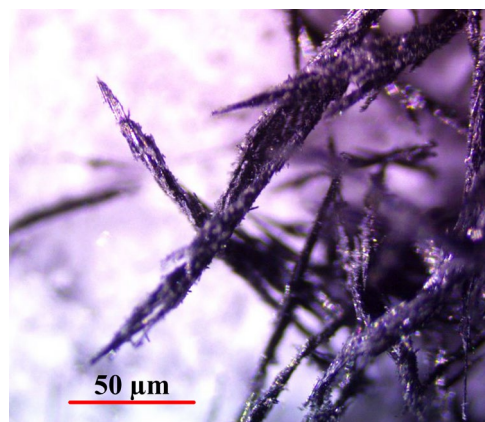
(a)

(b)



(c)

(d)



(e)

Fig. 4.6. Experimental chip formation in steady state cutting for $\theta=0^\circ$ and: (a) $i=0^\circ$, (b) $i=15^\circ$, (c) $i=30^\circ$, (d) $i=45^\circ$, (e) $i=60^\circ$.

At the fiber orientation of $\theta=45^\circ$ and tool inclination angle of $i=0^\circ$ (orthogonal cutting) in Fig. 4.7 (a), the fibers bend along their axes because of the excessive transverse compression in the contact region. The fibers first experience bending, followed by compressive failure due to the support of surrounding fibers. Since there is no oblique angle, chips are in the form of powder and are removed along the tool rake face. The average length of chips predicted by the FE simulations is around $15\ \mu\text{m}$, and more than 60% of the chips have the length ranging from 5 to $25\ \mu\text{m}$. Chip formation with tool inclination angle $i=30^\circ$ (oblique cutting) is shown in Fig. 4.7 (b). The mechanism of material removal remains the same. However, due to the oblique angle, the tool motion is able to remove the cracked fibers and matrix away from the contact zones, so the generated chips are in the form of longer rod-like chips, with average length of $40\ \mu\text{m}$. More than 65% of the chips have the length ranging from 28 to $55\ \mu\text{m}$. The collected chips from experiments for each case are shown in Fig. 4.8. The experimental figures show that the collected chips in orthogonal cutting are powder-like with an average size around $20\ \mu\text{m}$, and the collected chips in oblique cutting tend to be longer with an average size around $50\ \mu\text{m}$, and this trend is demonstrated from the FE simulation results.

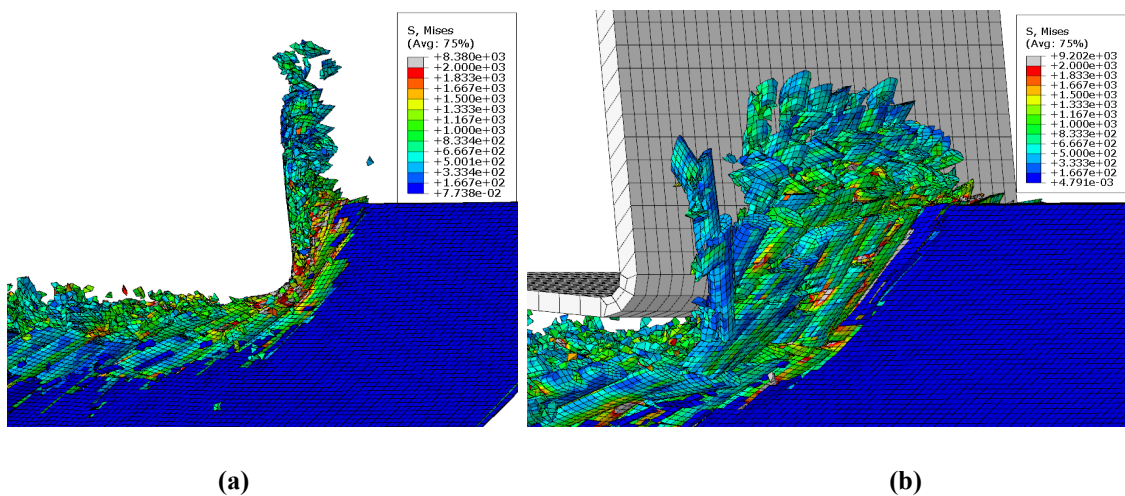
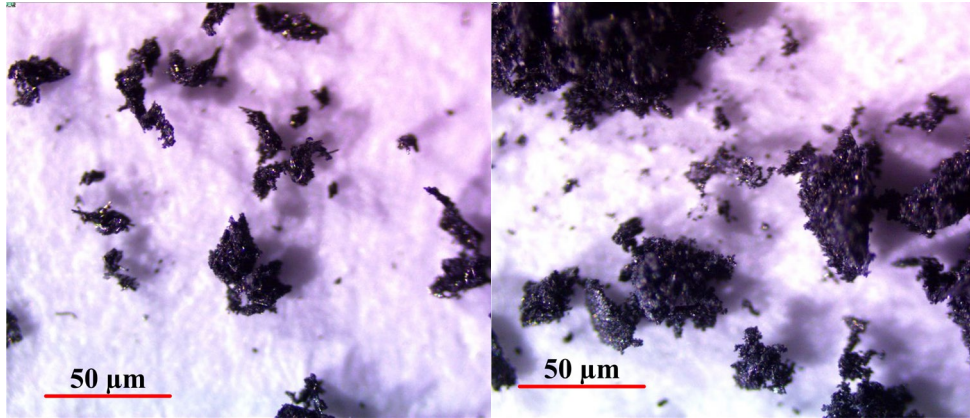
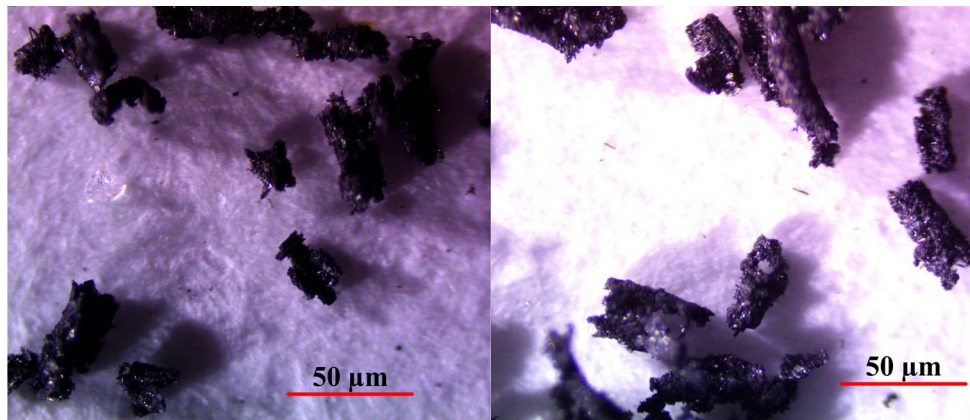


Fig. 4.7. Simulated chip formation in steady state cutting for: (a) $\theta=45^\circ$, $i=0^\circ$, (b) $\theta=45^\circ$, $i=30^\circ$.



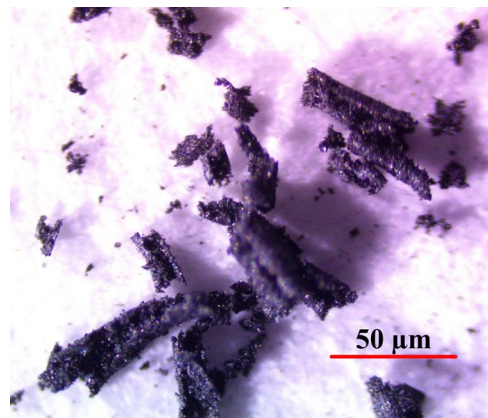
(a)

(b)



(c)

(d)



(e)

Fig. 4.8. Experimental chip formation in steady state cutting for $\theta=45^\circ$ and: (a) $i=0^\circ$, (b) $i=15^\circ$, (c) $i=30^\circ$, (d) $i=45^\circ$, (e) $i=60^\circ$.

For the case when $\theta = 90^\circ$ and $i = 0^\circ$ shown in Fig. 4.9 (a), as the tool penetrates into the workpiece, fiber bending occurs and the deformation zone ahead of the cutting tip is larger compared to the case of $\theta = 45^\circ$. Fiber fracture takes place across 3-4 fiber layers, which brings a deeper fiber – matrix debonding below the cutting tool edge. Chips are in the form of powder with average length of $15 \mu\text{m}$. When the tool inclination angle $i = 30^\circ$ as shown in Fig. 4.9 (b), chips are in the form of short rod-like chips and slide along the tool rake surface. More than 50% of the chips have the length ranging from 10 to $25 \mu\text{m}$. Typical chips collected from experiments for each case are shown in Fig. 4.10. In orthogonal cutting when $i = 0^\circ$, the collected chips are again powder-like, with the length ranging from $10 \mu\text{m}$ to $30 \mu\text{m}$. The average length is around $20 \mu\text{m}$. In oblique cutting when $i = 30^\circ$, the chips are in the form of a rod-like shape in the thickness direction, with an average thickness of $15 \mu\text{m}$. The maximum length in thickness direction is around $40 \mu\text{m}$, and the minimum length is less than $5 \mu\text{m}$. Overall, it is shown that the simulation results from the FE model are able to predict the trend of the chip length variation and chip morphology with respect to the fiber orientation and oblique angles according to the experimental examination.

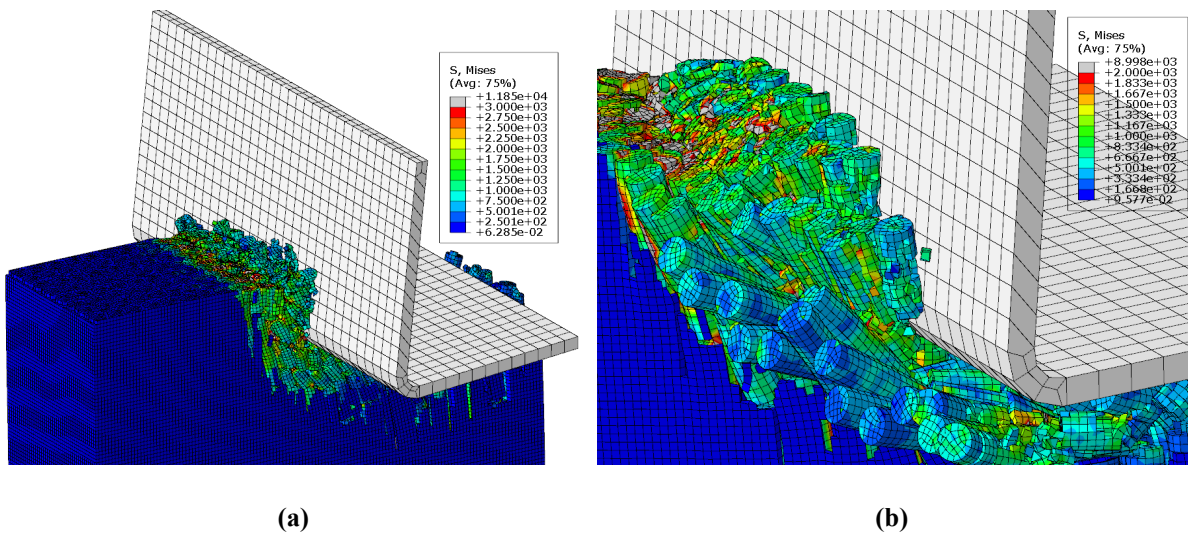
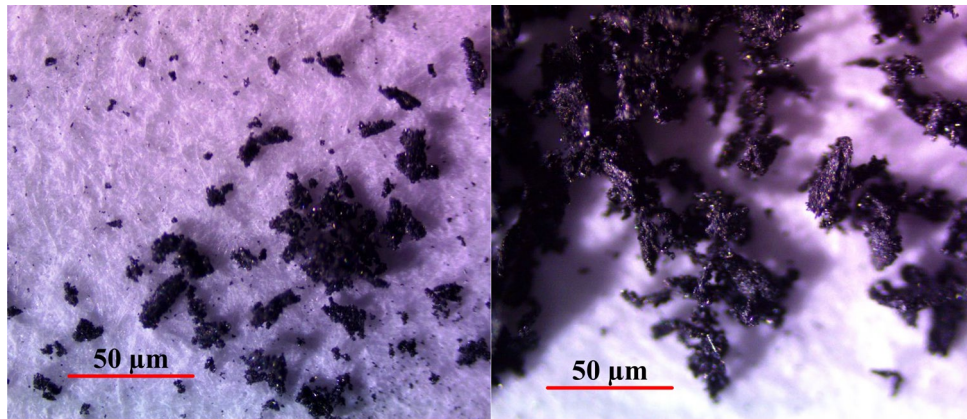
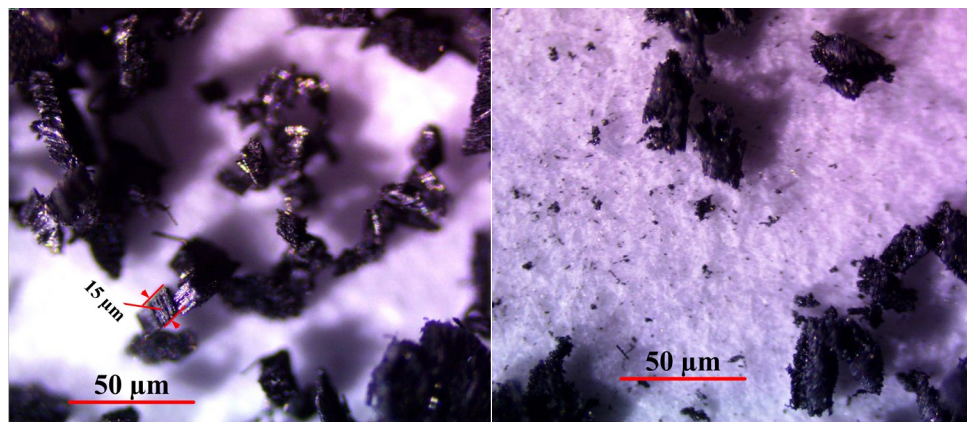


Fig. 4.9. Simulated chip formation in steady state cutting for: (a) $\theta=90^\circ$, $i=0^\circ$, (b) $\theta=90^\circ$, $i=30^\circ$.



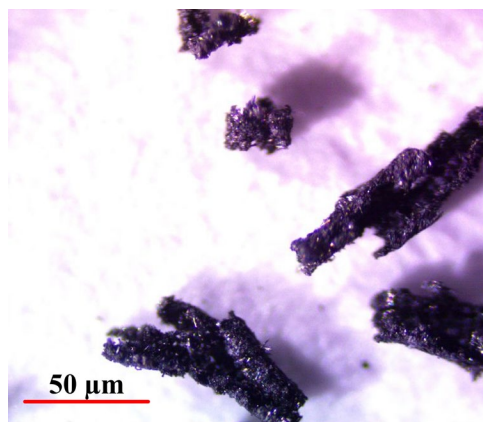
(a)

(b)



(c)

(d)



(e)

Fig. 4.10. Experimental chip formation in steady state cutting for $\theta=90^\circ$ and: (a) $i=0^\circ$, (b) $i=15^\circ$, (c) $i=30^\circ$, (d) $i=45^\circ$, (e) $i=60^\circ$.

4.2.2 Cutting forces

The cutting forces predicted by the FE simulations and the experiments are compared quantitatively. The time-domain cutting forces in tangential (F_c) and out-of-plane (F_r) directions are obtained. An example of the simulated cutting forces in the time domain at the fiber orientation angle of 45° and tool inclination angle of 30° are shown in Fig. 4.11. The force results are represented by the force per unit width (unit: N/mm). It is found that all the forces increase from zero to steady-state values, and the variation range of the forces is within 30% of the average values.

Fig. 4.12 shows the experimentally measured cutting forces [unit: N/mm] in the time domain, corresponding to the fiber orientation angle of 0° and oblique angle of 30° . The cutting forces almost keep constant during the steady-state cutting period, and the oscillation magnitudes are within 15% of the average values. The force oscillations are due to periodical fiber breakage and fibre/matrix fracture during the cutting process. A range of cutting speeds from 0.1 m/min to 10 m/min were investigated experimentally, and no obvious difference was found in the cutting forces.

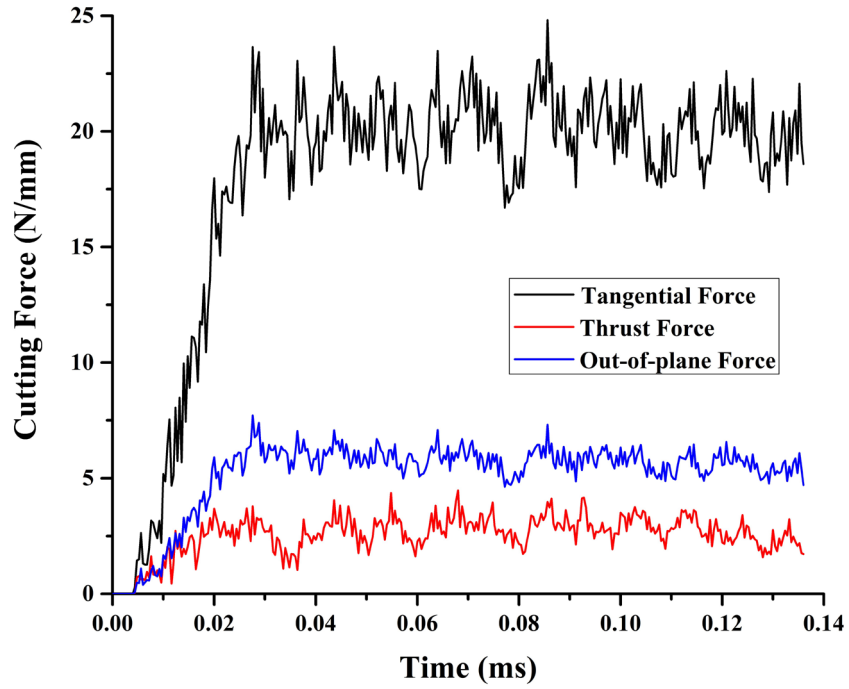


Fig 4.11. Cutting forces of fiber orientation $\theta=45^\circ$ and tool inclination angle $i=30^\circ$ in simulation.

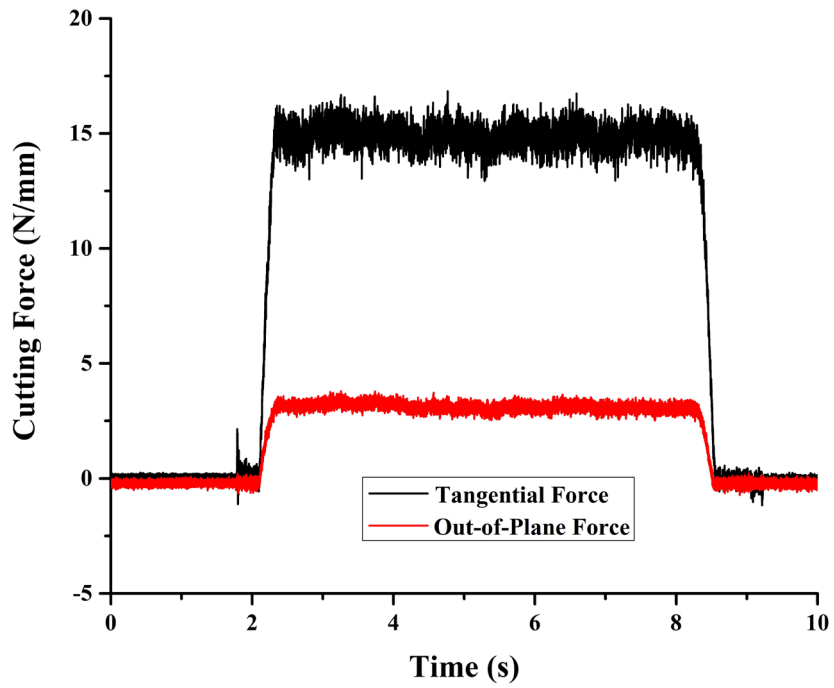


Fig 4.12. Cutting forces of fiber orientation $\theta=0^\circ$ and tool inclination angle $i=30^\circ$ in experiment.

The average force values obtained from FE simulations and cutting experiments at various fiber orientation angles and tool oblique angles are shown in Fig. 4.13-4.15. It should be noted that the cutting experiments were always performed on a pre-cut CFRP surface, therefore, the simulations only show the simulated force corresponding to the second tool pass for comparison purposes. The error bars show the variations of the forces in three repeated cutting tests.

When the fiber orientation angle is $\theta = 0^\circ$, the maximum difference ($\approx 48\%$) of tangential forces between simulation and experimental results is observed when tool inclination angle is 0° . The reason is that fibers are assumed to be linear elastic, and the maximum stress failure criterion is used in the FE simulation. Thus, when the tool inclination angle is less than 40° , fibers mainly experience buckling failure in the simulations. However, in the experiments, not all the fibers in the workpiece are perfectly aligned in the same direction, and the fibers may experience combined buckling and pure bending failure modes, resulting in lower tangential forces. When the tool inclination angle is larger, fibers are peeled up from the surface rather than experiencing compressive failure. Therefore, lower forces in the cutting direction and higher forces in the out-of-plane direction are observed compared to experimental forces, as shown in Fig. 4.13. The differences of tangential forces between the simulations and the experiments decrease to be smaller than 25% when the oblique angle is larger than 40° .

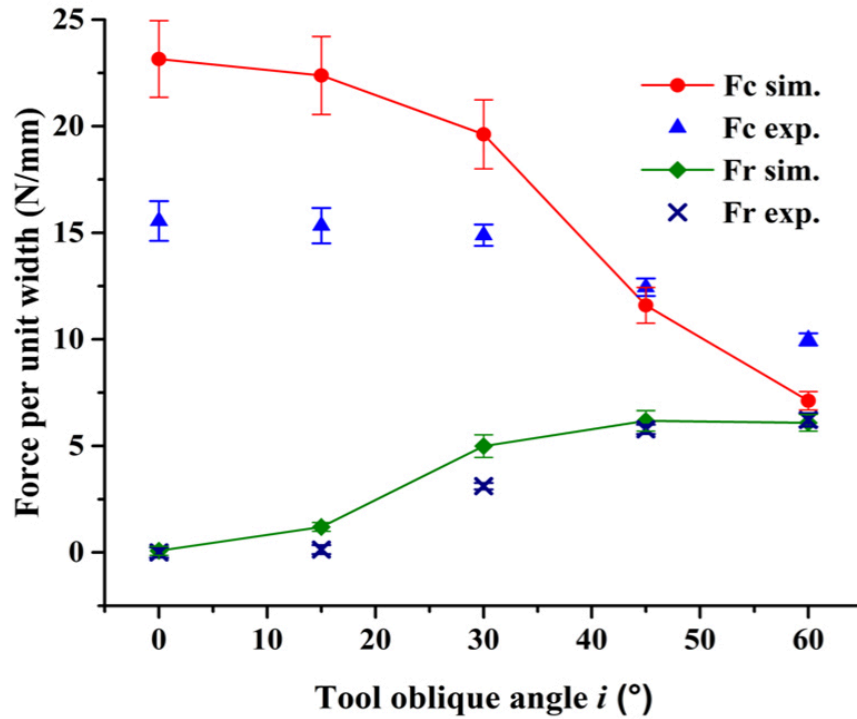


Fig. 4.13. Comparison between simulated and experimental forces with fiber orientation $\theta = 0^\circ$.

When fiber orientation angle is $\theta = 45^\circ$, it is shown that the predicted forces agree with the experimental measurement at different tool inclination angles, and the difference between the simulated and experimental cutting forces is less than 12%. Lower force in the cutting direction and higher force in the out-of-plane direction are observed in the simulations as shown in Fig. 4.14. When the oblique angle is 45° , out-of-plane force accounts for 42% of tangential force, and this proportion increases to 71% for 60° oblique angle. Note that out-of-plane force corresponds to the vertical force in drilling and milling, which is the main source of delamination between the CFRP layers. High cutting force in the vertical direction in milling and drilling may cause severe fiber delamination and lead to part damage.

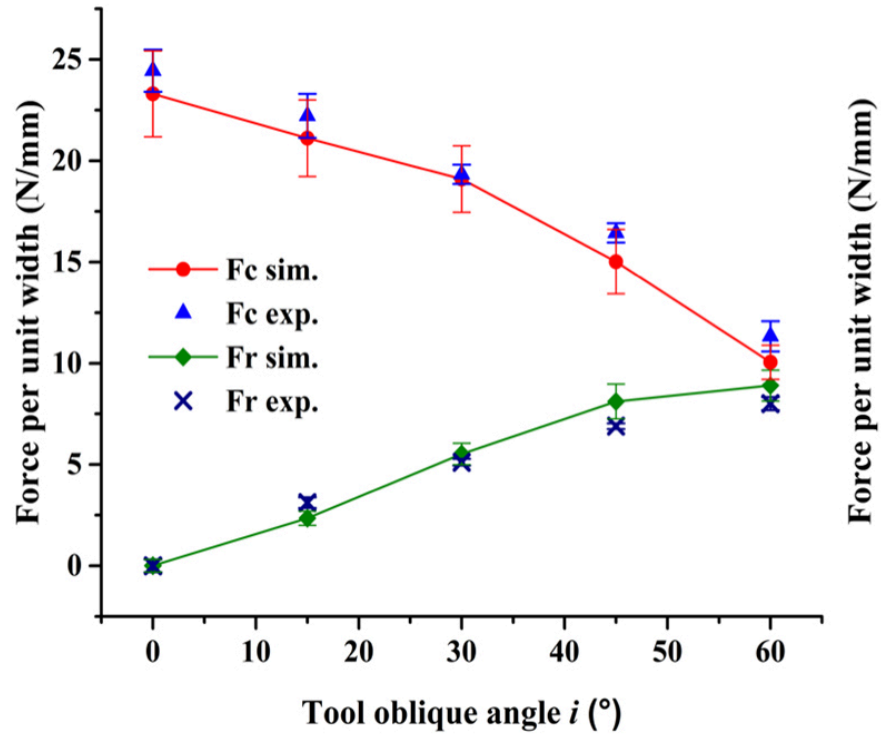


Fig. 4.14. Comparison between simulated and experimental forces with fiber orientation $\theta = 45^{\circ}$.

When the fiber orientation is $\theta = 90^{\circ}$, the tangential force in simulation has the largest variation of 57% when the tool inclination angle is 60° ; for out-of-plane force, the largest variation is 11%. With an increasing oblique angle, the forces in the tangential direction decrease while the forces in the out-of-plane direction increase, as shown in Fig. 4.15. This trend predicted in the simulations agrees with the experimental results. When oblique angles are 45° and 60° , the out-of-plane force accounts for 30% and 35% of the tangential force respectively, which are not negligible when evaluating the machining performance.

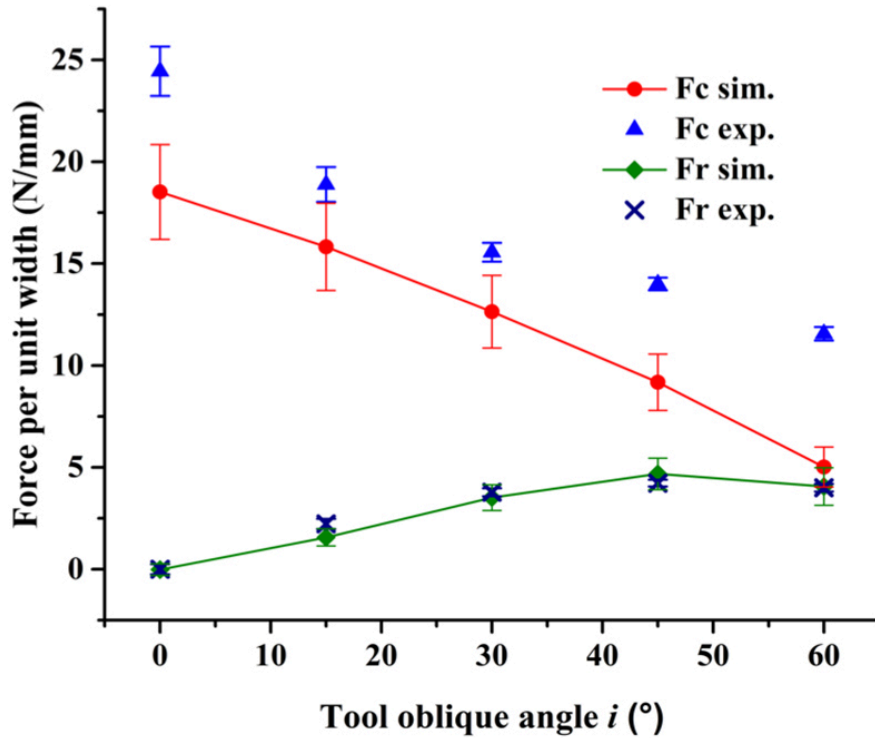


Fig. 4.15. Comparison between simulated and experimental forces with fiber orientation $\theta = 90^\circ$.

The comparison shows that the FE simulations are able to capture the trend and that the tangential forces decrease and the out-of-plane forces increase with the oblique angle for all fiber orientation angles tested. This is due to the out-of-plane fiber deformation and chip formation with the increase of oblique angle. In the experiments, because of the structure vibration and inherent defect of the specimen, not all the fibers are broken entirely after the first cutting path, therefore, the remaining fibers in the second cut result in higher tangential force compared to the simulation results.

Chapter 5: Analyses and discussions

Based on the developed FE model with experimental validation, this chapter provides a detailed analysis and discussion on how oblique angle and sequential cutting influence the surface generation, and how the arrangement of fiber distribution in the FE model influences the simulation results.

5.1 Effect of oblique angle on surface generation

(1) When the fiber orientation angle is 0° and oblique angle is small (from 0° and 15°), the small tool-workpiece contact area causes stress concentration, which results in brittle compressive failure in the workpiece material. A very thin subsurface damage layer ($\approx 30 \mu\text{m}$, i.e. 2-3 layers of fiber) was observed, which involves fibers breaking into several long pieces due to compression at the bottom of the cutting tool edge. However, even though fiber breakage occurs, the fibers still stay in their original direction and position, which results in a relatively smooth surface.

With increasing oblique angle (Fig. 5.1 (b, c)), most of the fibers are peeled off from the surface rather than experiencing compressive failure. It is observed that with larger oblique angle, due to the friction and pushing effect by cutting tool edge, fibers tend to be rolled to the direction of tool rake face, resulting in higher irregularity on machined surface compared to smaller oblique angles. However, the depth of subsurface damage changes to approximately $20 \mu\text{m}$. The reason is that the rolling effect makes the subsurface fibers roll out of their original position, thus reduces the extent of compression effect on the fiber layers below.

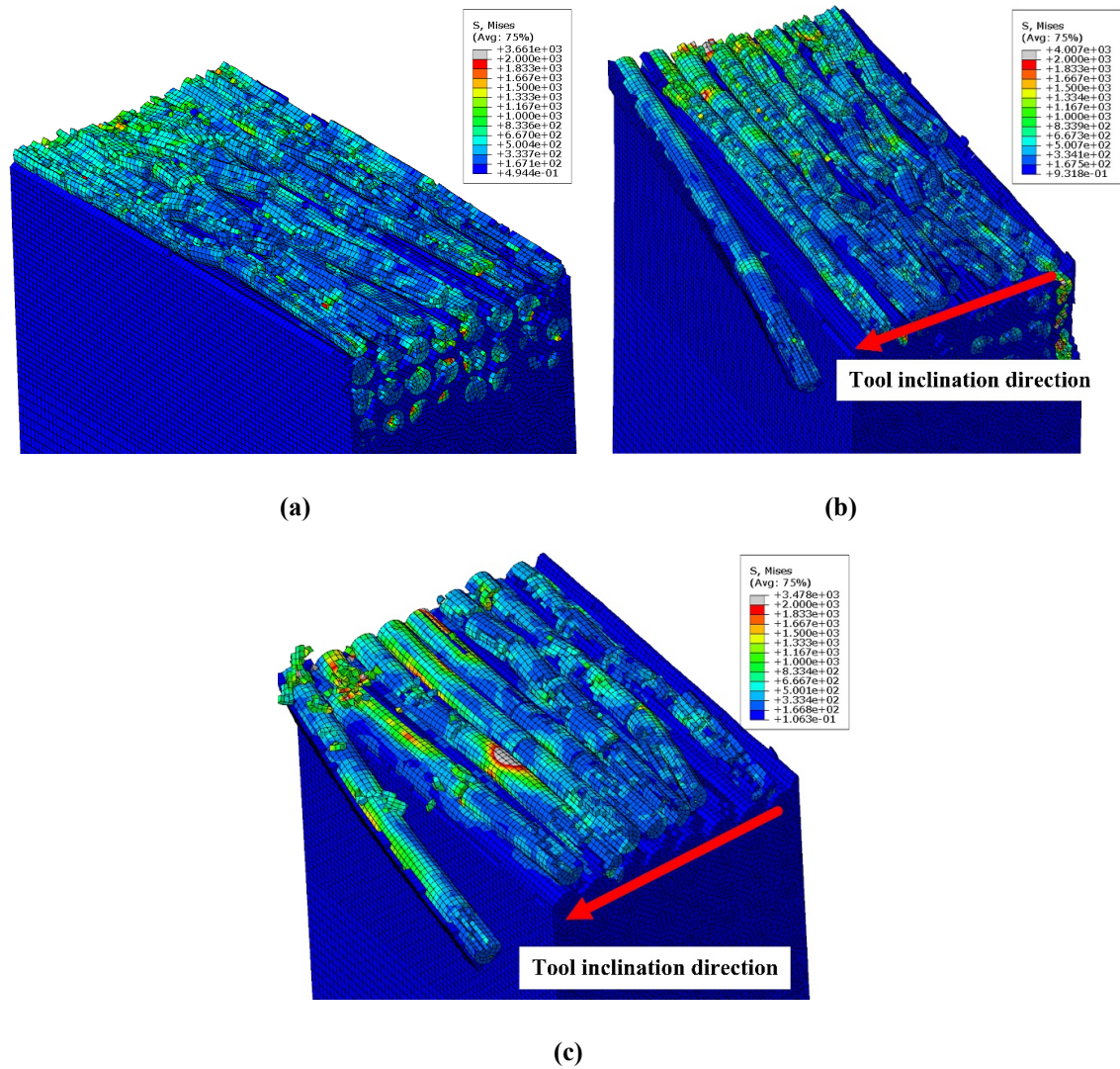


Fig. 5.1. Simulation results of the machined surface for (a) $\theta = 0^\circ, i = 0^\circ$, (b) $\theta = 0^\circ, i = 30^\circ$, (c) $\theta = 0^\circ, i = 45^\circ$.

(2) When the fiber orientation angle is $\theta = 45^\circ$ and the oblique angle is small ($0^\circ, 15^\circ$ and 30°), the cutting tool motion cannot instantly remove the broken fibers and matrix materials away from the contact zone. Therefore, some broken fibers and matrix materials remain on the generated surface. The direction of subsurface fibers keeps unchanged. The fibers on the top surface are at about the same height, as shown in Fig. 5.2 (a). Since a certain amount of unbroken matrix material still exists, most fibers are tightly packed to each other. The surface roughness is larger than that in 0°

fiber orientation angle. When the oblique angle is larger than 30° , the chips are removed along the tool rake face without experiencing further compressive failure. Therefore, less broken fibers and matrix materials remain on the generated surface, as shown in Fig. 5.2 (b) and (c). Due to the deformation of the fibers, most of the matrix materials have fractured, leaving gaps between the fibers. Moreover, since fibers at the subsurface are not broken completely, with the effect of friction subjected by tool flank face, the direction of subsurface fibers changes towards the tool rake face direction. This phenomenon may initiate delamination in actual machining process, because the fibers in outer layers have already been peeled up to a certain extent.

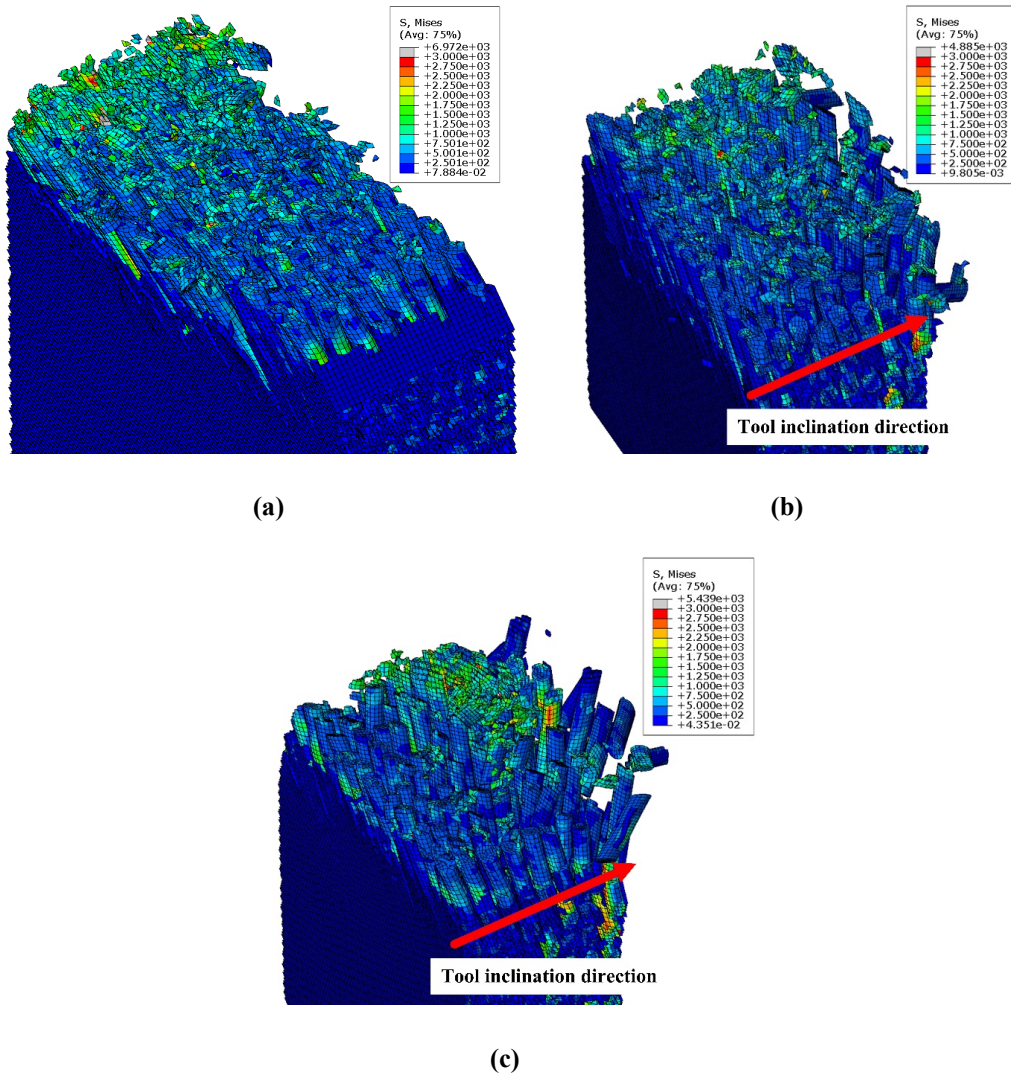
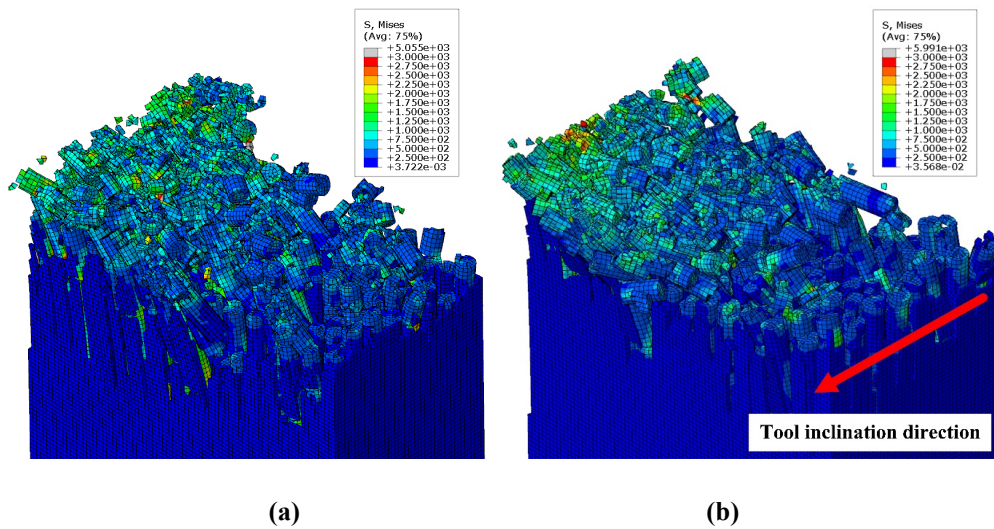
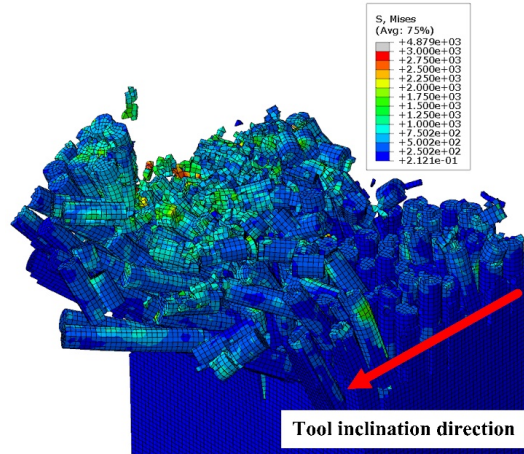


Fig. 5.2. Simulation results of the machined surface for (a) $\theta=45^\circ, i=0^\circ$, (b) $\theta=45^\circ, i=45^\circ$, (c) $\theta=45^\circ, i=60^\circ$.

(3) In cases of $\theta = 90^\circ$ fiber orientation angle and small oblique angles (0° and 30°), when the cutting tool contacts the fibers, the bending of fibers takes place across 4-5 fiber layers, which brings extensive fiber-matrix debonding below the cutting tool edge. Additionally, some of the fibers below the machined surface experience bending fracture caused by friction at the tool flank face. Thus, there are some gaps between the fibers as shown in Fig. 5.3 (a). The surface roughness is higher than that corresponding to the fiber orientation angles of $\theta = 0^\circ$ and $\theta = 45^\circ$. When the oblique angle is larger than 30° , fiber bending takes place across more layers of fiber, and fiber failure can be classified as combined compressive and bending modes. The fibers which are closer to the center of the tool edge experience compressive failure, because they are supported by surrounding fiber layers. The fibers that are closer to the side surface experience bending failure and are peeled off from the outer surface. Furthermore, the gaps between fibers observed in small oblique angle cases become larger when the oblique angle increases, resulting in larger surface roughness, as shown in Fig. 5.3 (c).





(c)

Fig. 5.3. Simulation result of the finished surface microstructure for the cutting with (a) $\theta=90^\circ$, $i=0^\circ$, (b) $\theta=90^\circ$, $i=30^\circ$, (c) $\theta=90^\circ$, $i=45^\circ$.

5.2 Effect of sequential cutting

The comparisons of the simulated machined surfaces between the first and the second cut at different oblique angles are shown in Fig. 5.4. The average forces obtained from the first and second cuts at various fiber orientations and oblique angles are compared in Fig. 5.5. For 0° fiber orientation angle, only the first two fiber layers under the tool edge are affected by the first cut. These fibers still stay in their original direction and position, resulting in similar cutting conditions for the second cutting pass. Therefore, the cutting forces in both tangential and out-of-plane directions are close between the first and the second cuts, as shown in Fig. 5.5 (a).

For 45° fiber orientation angle, after the first cut, the depth of subsurface damage can reach $50\ \mu\text{m}$ below the machined surface. However, the damage at each fiber occurs at one location (Fig. 5.4 (c)), and the fibers do not break entirely. Compared to the first cut, the maximum reduction of tangential force in the second cut is 19%, as shown in Fig. 5.5 (b), while the maximum reduction

of out-of-plane force 21%. The depth of subsurface damage and surface quality are similar between two sequential cutting.

For 90° fiber orientation angle, the depth of subsurface damage reaches beyond 70 μm after the first cut. Since excessive compression and friction force are applied by the tool edge and flank face, the fibers experience bending failure at different locations and break into several small pieces. Meanwhile, the matrix materials between the fibers also fail. During the second cutting process, short pieces of fibers are pushed forward by the tool rake face before the stress meets the maximum failure strength of the fibers. As a result, it is observed that the maximum reduction of tangential force in the second cut is 63% compared to the first cut. Meanwhile, out-of-plane force decreases by up to 68%. Moreover, the extent of subsurface damage and debonding produced by the second cut is up to 100 μm below the machined surface, which is more severe compared to the cases corresponding to the fiber orientation angles of 0° and 45°. The comparison of simulated subsurface damage depths between the first and second cuts at different fiber orientation angles are summarized and shown in Fig. 5.6.

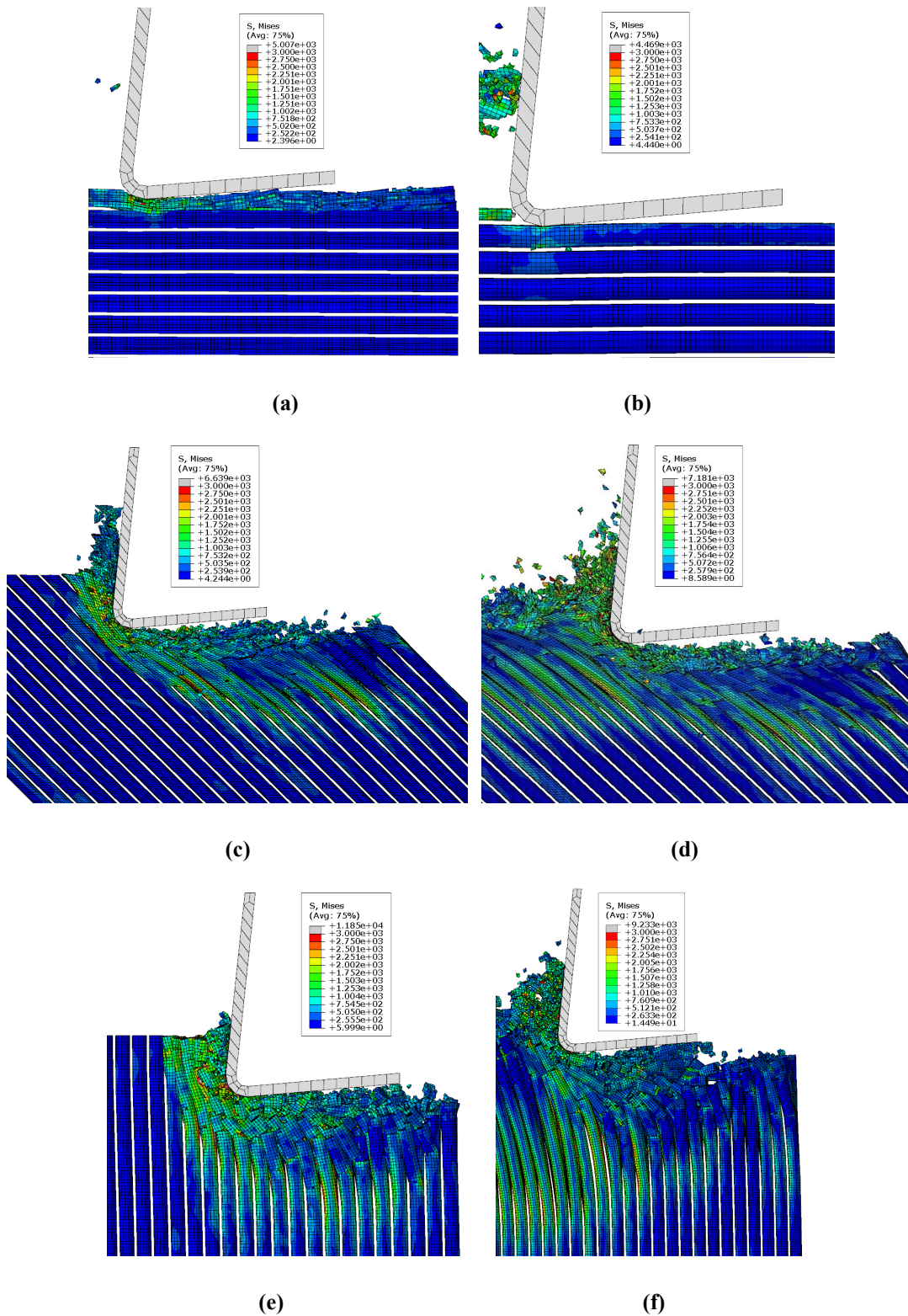


Fig. 5.4. Simulation results of the subsurface damage for: (a) $\theta = 0^\circ$, first cut, (b) $\theta = 0^\circ$, second cut, (c) $\theta = 45^\circ$, first cut, (d) $\theta = 45^\circ$, second cut, (e) $\theta = 90^\circ$, first cut, (f) $\theta = 90^\circ$, second cut.

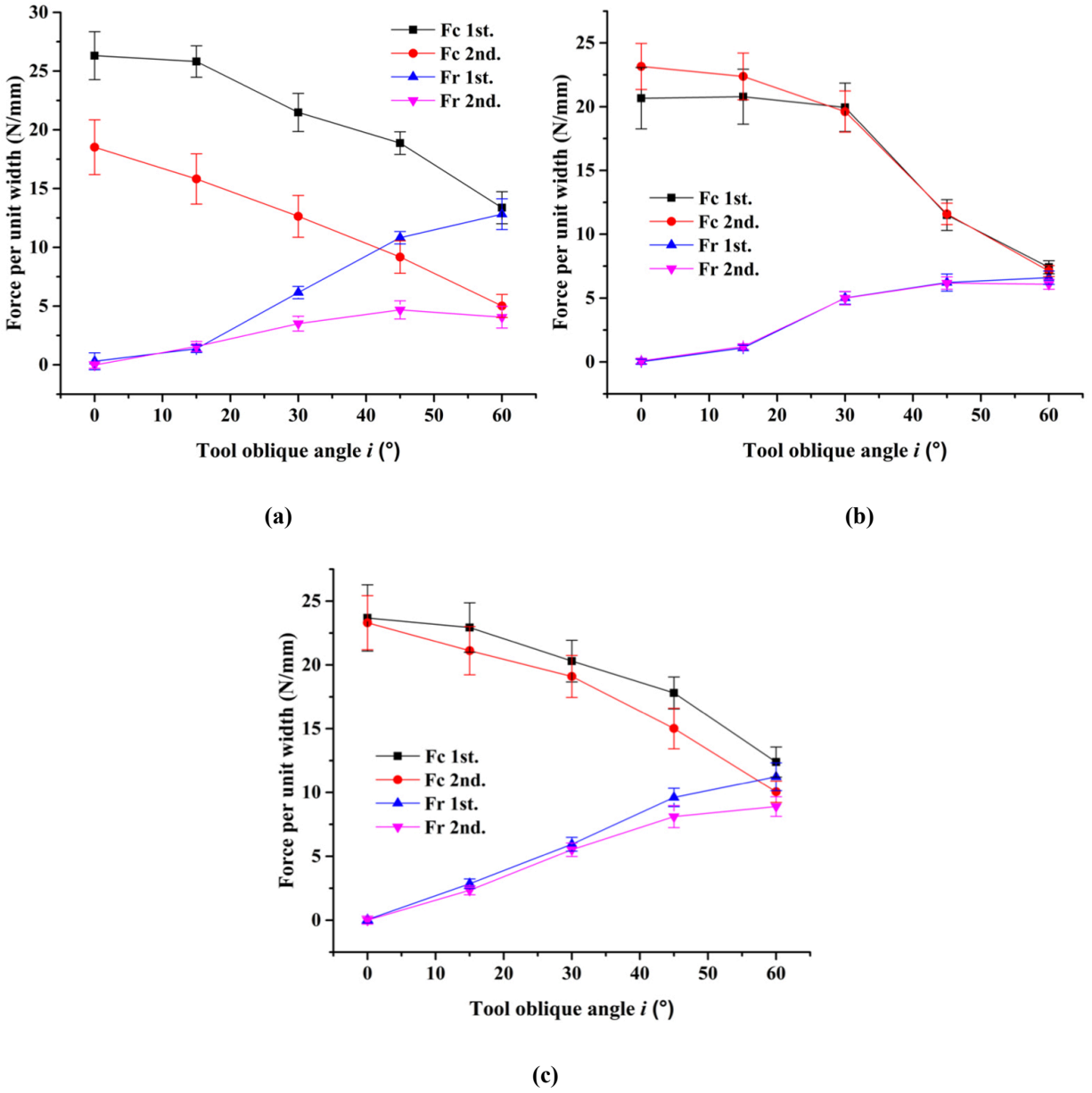


Fig. 5.5. Comparison of cutting forces between the first and the second cuts with fiber orientation angle: (a) $\theta = 0^\circ$, (b) $\theta = 45^\circ$, (c) $\theta = 90^\circ$. F_c represents the tangential force; F_r represents the out-of-plane force.

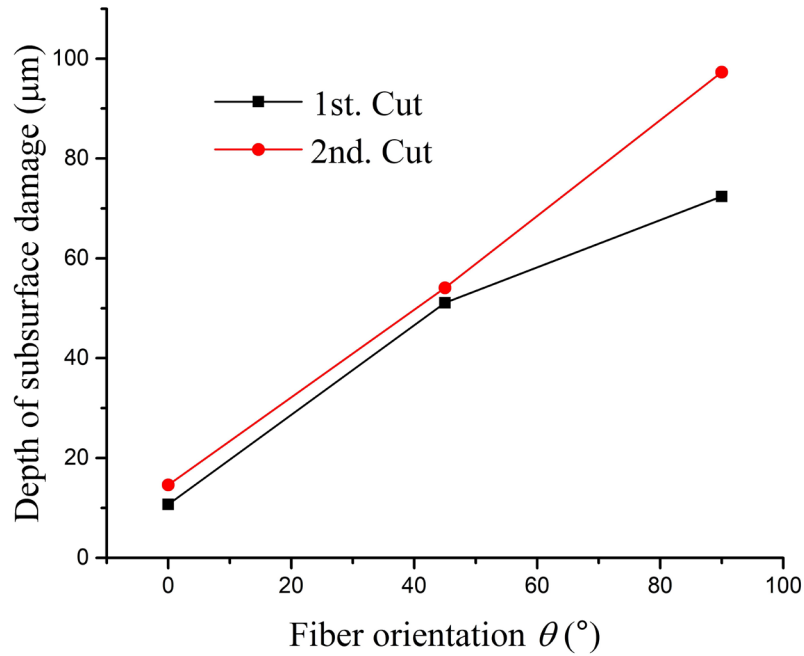


Fig. 5.6. Simulation results of the subsurface damage depth at different fiber orientation angles.

5.3 Effect of random fiber distribution on cutting forces

In actual CFRP composite materials, the arrangement of fibers is not in uniformly distributed as shown in Fig 3.1. (b). Therefore, a model with randomly distributed carbon fibers is established in order to perform sensitivity analysis on the effect of fiber distribution on the simulated cutting forces. Fig. 5.7 shows the schematics of the uniform and random fiber distributions in the FE model. FE simulations are conducted based on the CFRP workpiece with random fiber distribution, and the comparisons of the average cutting forces and the force oscillation amplitudes between uniform and random fiber arrangement are summarized in Table. 3. The cutting conditions are $\theta=45^\circ$ with $i=15^\circ$ and $i=45^\circ$ respectively. The maximum difference of the average force results is 6.1% from the simulation cases. This shows that the FE model with uniformly distributed fibers is

able to provide meaningful average force results. However, the force oscillation amplitudes with random fiber distribution are higher, due to the variation of fiber deformation modes at various locations.

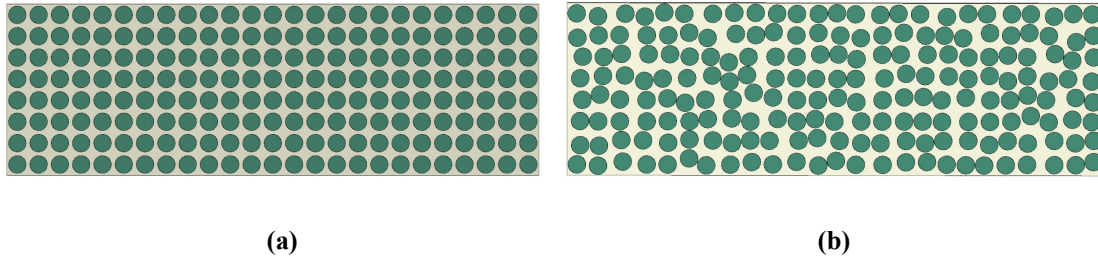


Fig. 5.7. Schematic illustration of (a) workpiece with uniform distributed fibers, (b) workpiece with random distributed fibers.

Table 3 Comparison of cutting forces between workpiece with uniform and random distribution of fibers for $\theta = 45^\circ$ and $i = 15^\circ$ and $i = 45^\circ$.

Oblique angle (i)	Force	Specific cutting force (N/mm)			Force oscillation amplitude (N/mm)	
		Uniform distribution	Random distribution	Difference	Uniform distribution	Random distribution
15°	$F_c, 1^{st}$ cut	22.93	21.54	6.1%	8.34	14.36
	$F_r, 1^{st}$ cut	2.85	2.89	1.4%	1.88	3.14
	$F_c, 2^{nd}$ cut	21.12	20.77	1.7%	7.96	15.30
	$F_r, 2^{nd}$ cut	2.34	2.45	4.7%	1.53	3.71
45°	$F_c, 1^{st}$ cut	17.81	17.04	4.3%	4.89	12.84
	$F_r, 1^{st}$ cut	9.61	9.49	1.2%	3.67	7.29
	$F_c, 2^{nd}$ cut	15.02	15.04	0.13%	5.09	13.45
	$F_r, 2^{nd}$ cut	8.11	8.15	0.49%	3.22	8.66

Chapter 6: Conclusion and future work

6.1 Conclusion

A 3-D FE model of machining UD-CFRP is developed to investigate the cutting mechanisms of fiber breakage, matrix cracking and fiber-matrix debonding at various fiber orientation and oblique angles. The results from oblique and sequential cutting of CFRP represent the actual tool-workpiece interaction in practical machining operations. The effects of the oblique angle and the subsurface damage on the cutting force and surface generation in subsequent cutting process are analyzed. The simulated forces are compared with the experimental results. The major conclusions from the simulations and the corresponding experimental analyses are given below:

(1) In all fiber orientation angles, the morphology of chip formation at small oblique angles tend to be powder-like or short rod-like shapes due to the compression of the cutting tool. In contrast, the lengths of the chips become longer because they are able to flow along the out-of-plane direction on tool rake face. The trend of chip length increase is also proved by experimental examinations on the machined chip morphology.

(2) Associated with the fiber deformation and chip formation in oblique cutting, the cutting force in the out-of-plane direction is generated, which contributes to potential delamination of CFRP in milling and drilling operations. When the oblique angle increases from 15° to 60° , the forces in the tangential direction decrease by 46% - 64%, and the forces in the out-of-plane direction increase by 160% - 502% based on the tested cases in this study. The sequential cutting simulations show that the first cut results in material damage below the machined surface, which causes the

reduction of forces in the second cutting. The comparison between the simulated and experimental force results prove that it is necessary to consider sequential cutting for the force predictions.

(3) Increasing the oblique angle causes more subsurface damages because the tool inclination angle changes the material mechanism from brittle compressive failure to bending failure of fibers, leading to further fiber-matrix debonding. Fibers move towards the tool inclination direction regardless of fiber orientation. Fiber delamination may occur with high oblique angles (45° and 90°) due to the out-of-plane deformation.

(4) Subsurface damage at 0° fiber orientation angle is the smallest compared to other angles. Therefore, there are no apparent differences of the cutting forces between the first and the second cuts. For 90° fiber orientation angle, severe subsurface damages caused by the first tool passing result in significant decrease of the cutting forces in the second cut.

(5) The simulation results with random fiber distribution in the FE model show that the configuration of the fiber arrangement does not significantly influence the average cutting forces, while the amplitudes of the force oscillations increase extensively due to the variations of the fiber deformation modes with random fiber distribution.

Overall, the proposed FE model on oblique and sequential cutting of CFRP reveals the effect of oblique cutting angle and multiple tool passes on the mechanisms of chip formation and surface generation, and predicts the cutting forces with experimental verification. The simulation results are able to provide guidance in choosing proper cutting parameters to minimize the delamination and subsurface damage in actual milling and drilling operations of CFRP composites.

6.2 Future work

(1) In the presented simulation results, only one uncut chip thickness and one tool geometry is considered due to the restriction of computational cost. This model can be extended to investigate the effects of uncut chip thickness and tool rake angle on the chip formation, cutting force and surface generation in oblique cutting of CFRP.

(2) In this thesis, both the simulations and the experiments are based on machining of CFRP in low cutting speed range (cutting speed is 0.5 m/min). In the future, the effects of strain-rate and temperature on the mechanical properties of matrix material in high-speed machining of CFRP will be considered. The constitutive property of matrix material including the combined effects of strain, strain-rate, and temperature will be included in the FE model.

(3) The friction coefficient defined in the FE model as a constant value of 0.3. However, the friction coefficient may vary with different fiber orientation angles. Therefore, further study could be performed to investigate the effect of the fiber orientation and temperature on the friction property between the cutting tool and the workpiece.

(4) In this study, the cutting tool was modeled as rigid body because it has higher elastic modulus than that of CFRP material. However, due to the extreme abrasiveness of carbon fiber, tool wear occurs in the cutting process, and changes the tool edge geometry. Thus, the tool wear effect could be considered in determining the performance of oblique cutting of CFRP.

Bibliography

- [1] Wang, Changying, et al. "Occurrence and formation mechanism of surface cavity defects during orthogonal milling of CFRP laminates." *Composites Part B: Engineering* 109 (2017): 10-22.
- [2] Yan, Xiaoye, et al. "A study of energy dissipating mechanisms in orthogonal cutting of UD-CFRP composites." *Composite Structures* 220 (2019): 460-472.
- [3] Sheikh-Ahmad, Jamal Y. *Machining of polymer composites*. Vol. 387355391. New York: Springer, 2009.
- [4] Song, Chunlei, and Xiaoliang Jin. "Shearing-buckling mechanism in orthogonal cutting of unidirectional carbon fiber reinforced polymer." *Journal of Materials Processing Technology* 280 (2020): 116612.
- [5] Tekkaya, A. E., et al. "Hot profile extrusion of AA-6060 aluminum chips." *Journal of materials processing technology* 209.7 (2009): 3343-3350.
- [6] Stabler, G. V. "The fundamental geometry of cutting tools." *Proceedings of the Institution of Mechanical Engineers* 165.1 (1951): 14-26.
- [7] Altintas, Yusuf, and A. A. Ber. "Manufacturing automation: metal cutting mechanics, machine tool vibrations, and CNC design." *Appl. Mech. Rev.* 54.5 (2001): B84-B84.
- [8] Everstine, G. C., and T. G. Rogers. "A theory of machining of fiber-reinforced materials." *Journal of Composite Materials* 5.1 (1971): 94-106.
- [9] Takeyama, H., and N. Iijima. "Machinability of glassfiber reinforced plastics and application of ultrasonic machining." *CIRP Annals* 37.1 (1988): 93-96.

- [10] Bhatnagar, N. B. A. I. I. O. T., et al. "On the machining of fiber reinforced plastic (FRP) composite laminates." *International journal of machine tools and manufacture* 35.5 (1995): 701-716.
- [11] Zhang, L. C., H. J. Zhang, and X. M. Wang. "A force prediction model for cutting unidirectional fibre-reinforced plastics." (2001): 293-305.
- [12] Zhang, Liangchi. *Solid mechanics for engineers*. Basingstoke, UK: Palgrave, 2001.
- [13] Johnson, Kenneth Langstreth, and Kenneth Langstreth Johnson. *Contact mechanics*. Cambridge university press, 1987.
- [14] Xu, Weixing, and L. C. Zhang. "On the mechanics and material removal mechanisms of vibration-assisted cutting of unidirectional fibre-reinforced polymer composites." *International Journal of Machine Tools and Manufacture* 80 (2014): 1-10.
- [15] Biot, M. "Bending of an Infinite Beam on an Elastic Substrate." *ASME J. Appl. Mech* 4 (1937): A1-A7.
- [16] Hetényi, Miklós. *Beams on elastic foundation: theory with applications in the fields of civil and mechanical engineering*. No. BOOK. University of Michigan, 1971.
- [17] Qi, Zhenchao, et al. "Microscopic mechanism based force prediction in orthogonal cutting of unidirectional CFRP." *The International Journal of Advanced Manufacturing Technology* 79.5-8 (2015): 1209-1219.
- [18] Winkler, E. "Theory of elasticity and strength." (1867): 77-93.
- [19] Voss, Robert, et al. "Analytical force model for orthogonal machining of unidirectional carbon fibre reinforced polymers (CFRP) as a function of the fibre orientation." *Journal of Materials Processing Technology* 263 (2019): 440-469.

- [20] KoPlev, A. A., Aa Lystrup, and T. Vorm. "The cutting process, chips, and cutting forces in machining CFRP." *composites* 14.4 (1983): 371-376.
- [21] Wang, D. H., M. Ramulu, and D. Arola. "Orthogonal cutting mechanisms of graphite/epoxy composite. Part I: unidirectional laminate." *International Journal of Machine Tools and Manufacture* 35.12 (1995): 1623-1638.
- [22] Wang, X. M, and L. C. Zhang. "An experimental investigation into the orthogonal cutting of unidirectional fibre reinforced plastics." *International journal of machine tools and manufacture* 43.10 (2003): 1015-1022.
- [23] Arola, D., and M. Ramulu. "Orthogonal cutting of fiber-reinforced composites: a finite element analysis." *International journal of mechanical sciences* 39.5 (1997): 597-613.
- [24] Mahdi, Mofid, and Liangchi Zhang. "A finite element model for the orthogonal cutting of fiber-reinforced composite materials." *Journal of materials processing technology* 113.1-3 (2001): 373-377.
- [25] Chamis, Christos C. "Simplified composite micromechanics equations for hygral, thermal and mechanical properties." (1983).
- [26] Lasri, L., M. Nouari, and M. El Mansori. "Modelling of chip separation in machining unidirectional FRP composites by stiffness degradation concept." *Composites Science and Technology* 69.5 (2009): 684-692.
- [27] Nayak, D., N. Bhatnagar, and P. Mahajan. "Machining studies of UD-FRP composites part 2: finite element analysis." *Machining Science and Technology* 9.4 (2005): 503-528.
- [28] Rao, G. Venu Gopala, P. Mahajan, and N. Bhatnagar. "Micro-mechanical modeling of machining of FRP composites–Cutting force analysis." *Composites science and technology* 67.3-4 (2007): 579-593.

- [29] Calzada, Kevin A., et al. "Modeling and interpretation of fiber orientation-based failure mechanisms in machining of carbon fiber-reinforced polymer composites." *Journal of Manufacturing Processes* 14.2 (2012): 141-149.
- [30] Xu, Weixing, L. C. Zhang, and Yongbo Wu. "Elliptic vibration-assisted cutting of fibre-reinforced polymer composites: understanding the material removal mechanisms." *Composites Science and Technology* 92 (2014): 103-111.
- [31] Xu, Weixing, and Liangchi Zhang. "A new approach to characterising the surface integrity of fibre-reinforced polymer composites during cutting." *Composites Part A: Applied Science and Manufacturing* 103 (2017): 272-282.
- [32] Abena, Alessandro, Sein Leung Soo, and Khamis Essa. "Modelling the orthogonal cutting of UD-CFRP composites: Development of a novel cohesive zone model." *Composite Structures* 168 (2017): 65-83.
- [33] Armarego, E. J. A., and R. C. Whitfield. "Computer based modelling of popular machining operations for force and power prediction." *Cirp Annals* 34.1 (1985): 65-69.
- [34] Cheng, Hui, et al. "A micro-scale cutting model for UD CFRP composites with thermo-mechanical coupling." *Composites Science and Technology* 153 (2017): 18-31.
- [35] Belingardi, Giovanni, et al. "Progressive damage analysis of a rate-dependent hybrid composite beam." *Composite Structures* 154 (2016): 433-442.
- [36] Jones, Robert M. *Mechanics of composite materials*. CRC press, 1998.
- [37] Littell, Justin D., et al. "Measurement of epoxy resin tension, compression, and shear stress–strain curves over a wide range of strain rates using small test specimens." *Journal of Aerospace Engineering* 21.3 (2008): 162-173.

- [38] Abena, Alessandro, Sein Leung Soo, and Khamis Essa. "A finite element simulation for orthogonal cutting of UD-CFRP incorporating a novel fibre-matrix interface model." *Procedia CIRP* 31 (2015): 539-544.
- [39] Rao, G. Venu Gopala, Puneet Mahajan, and Naresh Bhatnagar. "Machining of UD-GFRP composites chip formation mechanism." *Composites science and technology* 67.11-12 (2007): 2271-2281.
- [40] Chennakesavelu, Ganesh. *Orthogonal machining of uni-directional carbon fiber reinforced polymer composites*. Diss. Wichita State University, 2010.
- [41] ABAQUS, Abaqus. "6.14, Dassault Systèmes Simulia Corp." *Provid. RI, USA* (2014).
- [42] Vaughan, T. J., and C. T. McCarthy. "Micromechanical modelling of the transverse damage behaviour in fibre reinforced composites." *Composites Science and Technology* 71.3 (2011): 388-396.